Thermo-hydro-mechanical modeling of impermeable discontinuity in saturated porous media with X-FEM technique

A.R. Khoei *, S. Moallemi, E. Haghighat

Center of Excellence in Structures and Earthquake Engineering, Department of Civil Engineering, Sharif University of Technology, P.O. Box 11365-9313, Tehran, Iran

ARTICLE INFO

ABSTRACT

In this paper, the extended finite element method is presented for thermo-hydro-mechanical (THM) modeling of impermeable discontinuities in saturated porous media. The X-FEM technique is applied to the THM governing equations for the spatial discretization, followed by a generalized Newmark scheme for the time domain discretization. The displacement field is enriched by the Heaviside and crack tip asymptotic functions, and the pressure and temperature fields are enriched by the Heaviside and appropriate asymptotic functions. The process is accomplished by partitioning the domain with triangular sub-elements. Numerical examples are presented to demonstrate the capability of proposed technique in saturated porous soils.

© 2012 Elsevier Ltd. All rights reserved.

1. Introduction

Thermo-hydro-mechanical (THM) modeling in porous media is one of the most important subjects in geotechnical and environmental engineering. There are various mathematical formulations proposed by researchers for thermo-hydro-mechanical model of porous saturated–unsaturated media in the literature. A fully coupled numerical model to simulate the slow transient phenomena involving the heat and mass transfer in deforming porous media was developed by Gawin and Klemm [1] and Gawin et al. [2], in which the heat transfer was taken through the conduction and convection into the model. A model in terms of displacements, temperature, capillary pressure and gas pressure was proposed by Schrefler et al. [3] and Gawin and Schrefler [4] in partially saturated deformable porous medium, where the effects of temperature on capillary pressure was investigated for drying process of partially saturated porous media. A finite element formulation of multiphase fluid flow and heat transfer within a deforming porous medium was presented by Vaziri [5] in terms of displacement, pore pressure and temperature, and its application was demonstrated in one-dimensional thermal saturated soil layer. A fully coupled thermo-hydro-mechanical model was applied by Neaupane and Yamabe [6] to describe the nonlinear behavior of freezing and thawing of rock. A general governing equation was proposed by Rutqvist et al. [7] for coupled THM process in saturated and unsaturated geologic formations. An object-oriented finite element analysis was performed by Wang and Kolditz [8] in thermo-hydro-mechanical problems of porous media. A combined THM-damage model was presented by Gatmiri and Arson [9] on the basis of a suction-based heat, moisture transfer and skeleton deformation equations for unsaturated media. A thermal conductivity model of three-phase mixture of gas, water and solid was developed by Chen et al. [10] and Tong et al. [11,12] for simulation of thermo-hydro-mechanical processes of geological porous media by combining the effects of solid mineral composition, temperature, liquid saturation degree, porosity and pressure on the effective thermal conductivity of porous media. The THM model was proposed by Dumont et al. [13] for unsaturated soils, in which the effective

---

* Corresponding author. Tel.: +98 21 6600 5818; fax: +98 21 6601 4828.
  E-mail address: arkhoei@sharif.edu (A.R. Khoei).

Nomenclature

b	gravitational acceleration force
E	modulus of elasticity
c	heat capacity
D	material property of solid skeleton
$H(\boldsymbol{x})$	Heaviside jump function
I	identity tensor
k_f	permeability coefficient of the media
K_f	bulk modulus of fluid phase
K_S	bulk modulus of solid phase
K_T	bulk modulus of porous media
$\mathcal{k}_f$	heat conductivity matrix of fluid phase
$\mathcal{k}_s$	heat conductivity matrix of solid phase
$\mathcal{k}_{pI}$	heat conductivity matrix of phase I
n	porosity of mixture
$\mathbf{n}_d$	normal vector to the discontinuity
$\mathbf{n}_\Gamma$	normal vector to the external boundary
$N_i(\boldsymbol{x})$	standard shape function
p	pore pressure
q''	thermal flux
T	temperature
u	displacement of mixture
ü	acceleration of mixture
$\mathbf{v}_{pI}$	absolute velocity of phase I
$\mathbf{w}_f$	relative velocity of the fluid to solid phase
α	Biot coefficient
β	thermal expansion coefficient of bulk
β_f	thermal expansion coefficient of fluid
β_s	thermal expansion coefficient of solid
$\boldsymbol{\varepsilon}$	total strain
$\boldsymbol{\varepsilon}^t$	thermal strain
v	Poisson ratio
ρ	total density of mixture
ρ_f	density of fluid phase
ρ_s	density of solid phase
$\boldsymbol{\sigma}$	total stress
$\boldsymbol{\sigma}'$	effective stress
$\varphi(\boldsymbol{x})$	field variable
$\Phi^j(\boldsymbol{x})$	tip asymptotic functions

stress is extended to unsaturated soils by introducing the capillary pressure based on a micro-structural model and taking the effects of desaturation and thermal softening phenomenon into the model.

Modeling of discontinuity with finite element method in fractured/fracturing porous media has been attracted by researchers. One of the earlier research works in THM modeling of two-phase fractured media was illustrated by Noorishad et al. [14], where a numerical approach was given for the saturated fractured porous rocks. Boone and Ingraffea [15] presented a numerical procedure for the simulation of hydraulically-driven fracture propagation in poroelastic materials combining the finite element method with the finite difference method. A cohesive segments method was proposed by Remmers et al. [16] for the simulation of crack growth, where the cohesive segments were inserted into finite elements as discontinuities in the displacement field by exploiting the partition-of-unity property. Schrefler et al. [17] and Secchi et al. [18] modeled the hydraulic cohesive crack growth problem in fully saturated porous media using the finite element method with mesh adaptation. The crack propagation simulation was performed by Radi and Loret [19] for an elastic isotropic fluid-saturated porous media at an intersonic constant speed. Hoteit and Firoozabadi [20] proposed a numerical procedure for the incompressible fluid flow in fractured porous media based on the combination of finite difference, finite volume and finite element methods. Segura and Carol [21] proposed a hydro-mechanical formulation for fully saturated geomaterials with pre-existing discontinuities based on the finite element method with zero-thickness interface elements. The cohesive segment method was employed by Remmers et al. [22] in dynamic analysis of the nucleation, growth and coalescence of multiple cracks in brittle solids. Khoei et al. [23] and Barani et al. [24] presented a dynamic analysis of cohesive fracture propagation in saturated and partially saturated porous media. The importance of cohesive zone model

in fluid driven fracture was studied by Sarris and Papanastasiou [25], and it was shown that the crack mouth opening has larger value in the case of elastic-softening cohesive model compared to the rigid softening model. A numerical model based on the fully coupled approach was presented by Carrier and Granet [26] for the hydraulic fracturing of permeable medium, where four limiting propagation regimes were assumed.

In modeling of discontinuity based on the standard FEM, the discontinuity is restricted to the inter-element boundaries suffering from the mesh dependency. In such case, the successive remeshing must be carried out to overcome the sensitivity to FEM mesh that makes the computation expensive and cumbersome process. The difficulties confronted in the standard FEM are handled by locally enriching the conventional finite element approximation with an additional function through the concept of the partition of unity, which was introduced in the pioneering work of Melenk and Babuska [27]. The idea was exploited to set up the frame of the extended finite element method by Belytschko and Black [28] and Moës et al. [29]. Indeed, the extended finite element approximation relies on the partition of unity property of finite element shape functions for the incorporation of local enrichments into the classical finite element basis. By appropriately selecting the enrichment function and enriching specific nodal points through the addition of extra degrees-of-freedom relevant to the chosen enrichment function to these nodes, the enriched approximation would be capable of directly capturing the local property in the solution [30–32]. The X-FEM was originally applied in mesh-independent crack propagation problems, including: the crack growth with frictional contact [33], cohesive crack propagation [34–36], stationary and growing cracks [37] and three-dimensional crack propagation [38]. An overview of the technique was addressed by Bordas et al. [39] in the framework of an object-oriented-enriched finite element programming. The technique was then employed in elasto-plasticity problems, including: the crack propagation in plastic fracture mechanics [40], the plasticity of frictional contact on arbitrary interfaces [41,42], the plasticity of large deformations [43–45] and the strain localization in higher-order Cosserat theory [46]. The X-FEM technique was extended to couple problems by its application in multi-phase porous media. The technique was proposed by de Borst et al. [47] and Rethore et al. [48] for the fluid flow in fractured porous media. The technique was employed in modeling of arbitrary interfaces by Khoei and Haghighat [49] in the non-linear dynamic analysis of deformable porous media. The method was proposed by Ren et al. [50] in modeling of hydraulic fracturing in concrete by imposing a constant pressure value along the crack faces. The technique was also employed by Lecamipon [51] in hydraulic fracture problems using the special crack-tip functions in the presence of internal pressure inside the crack. The X-FEM was recently employed by Mohamadnejad and Khoei [52,53] in hydro-mechanical modeling of deformable, progressively fracturing porous media interacting with the flow of two immiscible, compressible wetting and non-wetting pore fluids.

In the present study, the X-FEM technique is presented in thermo-hydro-mechanical modeling of impermeable discontinuities in saturated porous media. The governing equations of thermo-hydro-mechanical porous media is discretized by the X-FEM for the spatial discretization, and followed by a generalized Newmark scheme for time domain discretization. The impermeable discontinuity is modeled by the Heaviside and appropriate asymptotic tip enrichment functions for displacement, pressure, and temperature fields. The outline of the paper is as follows; the governing equations of thermo-hydro-mechanical porous media are presented in Section 2. Section 3 demonstrates the discontinuity behavior of displacement, pressure and temperature in THM medium. The weak form of governing equations are presented in Section 4 together with the spatial and time domain discretization of THM equations on the basis of the X-FEM and generalized Newmark approaches. In Section 5, several numerical examples are analyzed to demonstrate the efficiency of proposed model in saturated porous media. Finally, Section 6 is devoted to conclusion remarks.

2. Thermo-hydro-mechanical governing equations of saturated porous media

In order to derive the governing equations of thermo-hydro-mechanical porous media, the Biot theory is employed in saturated medium, which is coupled with the heat transfer analysis. The effective stress is an essential concept in the deformation of porous media, which can be defined by $\boldsymbol{\sigma}' = \boldsymbol{\sigma} + \alpha p \mathbf{I}$, where $\boldsymbol{\sigma}'$ and $\boldsymbol{\sigma}$ are the effective stress and total stress, respectively, $\mathbf{I}$ is the identity tensor and p is the pore pressure. In this relation, α is the Biot coefficient related to the material properties and defined by $\alpha = 1 - K_T/K_S$, where K_T and K_S are the bulk modulus of porous media and its solid grains, respectively, and it is assumed as $\alpha = 1$ for most soils. By neglecting the acceleration of fluid particles with respect to the solids, the linear momentum balance of solid–fluid mixture can be written as

$$\text{div } \boldsymbol{\sigma} - \rho \ddot{\mathbf{u}} + \rho \mathbf{b} = \mathbf{0} \tag{1}$$

where $\ddot{\mathbf{u}}$ is the acceleration of mixture, $\mathbf{b}$ is the gravitational acceleration and ρ is the total density of mixture defined as $\rho = n\rho_f + (1-n)\rho_s$, with ρ_f and ρ_s denoting the density of fluid and solid phases, respectively, and n is the porosity of mixture defined as the ratio of pore space to the total volume in a representative elementary volume.

In order to derive the mass balance equation of the mixture, the density of mixture is applied to each phase of domain as

$$\frac{\partial \rho_{pI}}{\partial t} + \nabla \cdot (\rho_{pI} \mathbf{v}_{pI}) = 0 \tag{2}$$

where $\mathbf{v}_{pI}$ denotes the absolute velocity of phase I in the bulk. Considering the solid–fluid mixture as a homogenous domain, Eq. (2) can be rewritten as

$$\frac{1-n}{\rho_s}\frac{\partial\rho_s}{\partial t} + \nabla\cdot\mathbf{v}_s + \frac{n}{\rho_f}\frac{\partial\rho_f}{\partial t} + n\nabla\cdot\mathbf{w}_f = 0 \tag{3}$$

where $\mathbf{w}_f$ is the relative velocity of the fluid to the solid phase. In order to derive the variation of fluid density with respect to time, ρ_f is defined by $\rho_f = \rho_{f_0}\exp[-\beta_f T + 1/K_f(p-p_0)]$ as described by Fernandez [54], where β_f is the volumetric thermal expansion coefficient of fluid, T is the temperature, and K_f is the bulk module of the fluid phase. Considering the solid density as a function of the temperature, pressure and the first invariant of effective stress [55], the mass balance equation of the mixture can be obtained as

$$\left(\frac{\alpha-n}{K_s} + \frac{n}{K_f}\right)\dot{p} - ((\alpha-n)\beta_s + n\beta_f)\dot{T} + \alpha\nabla\cdot\mathbf{v}_s + n\nabla\cdot\mathbf{w}_f = 0 \tag{4}$$

By applying the Darcy law into Eq. (4), the fluid velocity can be described in term of the pressure gradient in the isotropic porous medium that results in

$$\alpha\nabla\cdot\mathbf{v}_s + \nabla^T[k_f(-\nabla p + \rho_f\mathbf{b})] + \frac{\dot{p}}{Q^*} - \beta\dot{T} = 0 \tag{5}$$

where k_f is the permeability coefficient of the media, β is the thermal expansion coefficient of the bulk defined as $\beta = (\alpha - n)\beta_s + n\beta_f$ and $1/Q^* = (\alpha - n)/K_s + n/K_f$.

In order to derive the thermo-hydro-mechanical formulation, the heat transfer formulation is incorporated into the governing equations of porous saturated media using the energy conserving equation (enthalpy balance) for each phase. The governing equation of heat conduction is derived for a continuous medium from the principle of conservation of heat energy over an arbitrary fixed volume. Based on this principle, the heat increase rate of the system is equal to the summation of heat conduction and heat generation rate in a fixed volume. Applying the Fourier law of heat conduction, the energy balance equation can be written as

$$(\rho c)_{pI}\frac{\partial T}{\partial t} + (\rho c)_{pI}\mathbf{v}_{pI}\nabla T - \nabla\cdot(\pmb{k}_{pI}\nabla T) = 0 \tag{6}$$

where c denotes the heat capacity, and $\pmb{k}_{pI}$ is the heat conductivity matrix of phase I. Multiplying the energy equation (6) by its porosity for each phase, neglecting the velocity of solid phase as employed in [55], and using the Darcy law for the fluid velocity, the energy equation for the mixture can be obtained as

$$(\rho c)_{avg}\frac{\partial T}{\partial t} + (\rho_f c_f[k_f(-\nabla p + \rho\mathbf{b})])\nabla T - \nabla\cdot(\pmb{k}\nabla T) = 0 \tag{7}$$

where $(\rho c)_{avg} = (1-n)(\rho c)_s + n(\rho c)_f$ and $\pmb{k} = (1-n)\pmb{k}_s + n\pmb{k}_f$. The second term of Eq. (7) implies the effect of fluid flow on the heat transfer, as a convection term.

3. Discontinuities in THM medium

The singularity in a discontinuous porous media can be caused due to the thermal and pressure loading in the vicinity of singular points. Since the governing equation of fluid flow in porous media are similar to the heat transfer equation, the treatment of thermal field near the singular points is assumed to be similar to the fluid phase. By neglecting the effect of transient terms in the heat transfer equation at the vicinity of singular points, Eq. (7) can be transformed to $\nabla^2 T = 0$ in
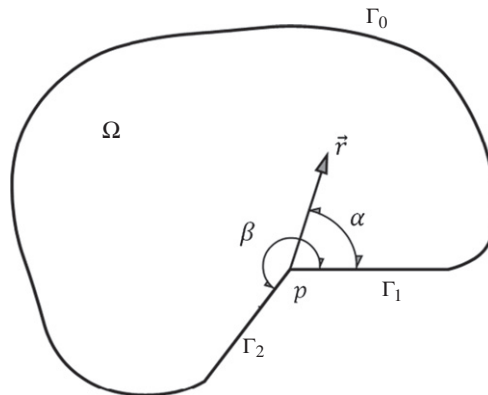

Fig. 1. Geometry of singularity. The domain Ω contains a reentrant corner with an internal angle β.

the absence of heat source, which is also valid near the discontinuity. In order to solve the heat transfer equation $\nabla^2 T = 0$, the boundary conditions must be applied at the discontinuity edges, as shown in Fig. 1. The boundary conditions near the singular point p is considered as one of the following cases

$$T(x,y) = 0 \quad (x,y) \in \Gamma_1, \Gamma_2 \quad \text{Dirichlet BC} \tag{8}$$

$$\frac{\partial T(x,y)}{\partial n} = 0 \quad (x,y) \in \Gamma_1, \Gamma_2 \quad \text{Neumann BC} \tag{9}$$

$$\begin{aligned} T(x,y) = 0 \quad (x,y) \in \Gamma_1 \\ \frac{\partial T(x,y)}{\partial n} = 0 \quad (x,y) \in \Gamma_2 \end{aligned} \quad \text{Dirichlet \& Neumann BCs} \tag{10}$$

The above boundary conditions can be used to solve the heat transfer equation near the singularity. The solution of the differential equation is given as [56]

$$T(r,\alpha) = \sum_{n=1}^{\infty} b_n r^{\frac{n\pi}{\beta}} \sqrt{\frac{2}{\beta}} \sin\left(\frac{n\pi\alpha}{\beta}\right) \quad \text{Dirichlet BC} \tag{11}$$

$$T(r,\alpha) = \sum_{n=0}^{\infty} b_n r^{\frac{n\pi}{\beta}} \cos\left(\frac{n\pi\alpha}{\beta}\right) \quad \text{Neumann BC} \tag{12}$$

$$T(r,\alpha) = \sum_{n=1}^{\infty} b_n r^{\frac{n\pi}{2\beta}} \sqrt{\frac{2}{\beta}} \sin\left(\frac{n\pi\alpha}{2\beta}\right) \quad \text{Dirichlet \& Neumann BCs} \tag{13}$$

where $0 \leqslant \alpha \leqslant 2\pi$. In the case of thermal discontinuity, the thermal flux on the discontinuity Γ_1 and Γ_2 is equal to zero, so the Neumann boundary condition must be applied on discontinuity faces and relation (12) is used as the near tip singular solution [57–59].

The same procedure can be applied to obtain the pressure distribution in the vicinity of singular point. Considering the Darcy equation as $\mathbf{w}_f = k_f(-\nabla p + \rho \mathbf{b})$ and the continuity equation as $\text{div}(\mathbf{w}_f) = 0$, the pressure differential equation can be obtained in the absence of gravity forces as

$$\nabla^2 p = 0 \tag{14}$$

This equation is similar to the partial differential equation derived for the steady-state thermal condition. In the case of impermeable discontinuity, the leak-off from the discontinuity faces is equal to zero. Thus, the solution of partial differential equation (14) at the singular point p can be obtained similar to relation (12) for the impermeable boundary condition as

$$P(r,\alpha) = \sum_{n=0}^{\infty} b_n r^{\frac{n\pi}{\beta}} \cos\left(\frac{n\pi\alpha}{\beta}\right) \tag{15}$$

and the fluid flow and thermal flux can be obtained by taking the derivation from (12) or (15) with respect to r and inserting $\beta = 2\pi$ as

$$q(r,\alpha) = \sum_{n=0}^{\infty} c_n r^{\frac{n}{2}-1} \cos\left(\frac{n\alpha}{2}\right) \hat{e}_r - \sum_{n=0}^{\infty} c_n r^{\frac{n}{2}-1} \sin\left(\frac{n\alpha}{2}\right) \hat{e}_\alpha \tag{16}$$

The above relation presents the singularity of fluid and thermal fluxes in the vicinity of point p.

4. Extended-FEM formulation of THM governing equations

In order to derive the weak form of governing equations (1), (4) and (7), the trial functions $\mathbf{u}(\boldsymbol{x},t)$, $p(\boldsymbol{x},t)$, $T(\boldsymbol{x},t)$ and the test functions $\delta\mathbf{u}(\boldsymbol{x},t)$, $\delta p(\boldsymbol{x},t)$ and $\delta T(\boldsymbol{x},t)$ are required to be smooth enough in order to satisfy all essential boundary conditions and define the derivatives of equations. Furthermore, the test functions $\delta\mathbf{u}(\boldsymbol{x},t)$, $\delta p(\boldsymbol{x},t)$ and $\delta T(\boldsymbol{x},t)$ must be vanished on the prescribed strong boundary conditions. To obtain the weak form of governing equations, the test functions $\delta\mathbf{u}(\boldsymbol{x},t)$, $\delta p(\boldsymbol{x},t)$ and $\delta T(\boldsymbol{x},t)$ are multiplied by Eqs. (1), (4) and (7), respectively, and integrated over the domain Ω as

$$\begin{aligned} &\int_\Omega \delta\mathbf{u}(\text{div}\boldsymbol{\sigma} - \rho\ddot{\mathbf{u}} + \rho\mathbf{b})d\Omega = 0 \\ &\int_\Omega \delta p(\alpha\nabla \cdot \mathbf{v}_s + \nabla^T[k_f(-\nabla p + \rho\mathbf{b})] - \beta\dot{T})d\Omega = 0 \\ &\int_\Omega \delta T((\rho c)_{avg}\dot{T} + (\rho_f c_f[k_f(-\nabla p + \rho\mathbf{b})])\nabla T - \mathcal{K}\nabla^2 T)d\Omega = 0 \end{aligned} \tag{17}$$
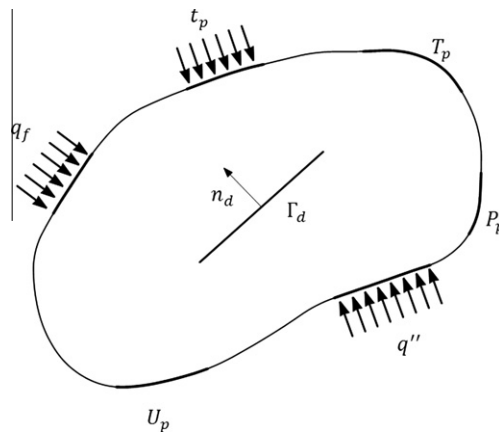
Fig. 2. Geometry of discontinues domain and its boundary conditions.

Expanding the integral equations (17) and applying the Divergence theorem, leads to the following weak form of governing equations

$$\int_\Omega \delta\mathbf{u}\rho\ddot{\mathbf{u}}\,d\Omega + \int_\Omega (\nabla\delta\mathbf{u})^T : \boldsymbol{\sigma}\,d\Omega = \int_\Omega \delta\mathbf{u}\rho\mathbf{b}\,d\Omega + \int_\Gamma \delta\mathbf{u}\bar{\mathbf{t}}\,d\Gamma$$

$$\int_\Omega \delta p\alpha\nabla\cdot\mathbf{v}_s\,d\Omega + \int_\Omega \nabla\delta p k_f\nabla p\,d\Omega + \int_\Omega \delta p\frac{1}{Q}\dot{p}\,d\Omega - \int_\Omega \delta p\beta\dot{T}\,d\Omega = \int_\Gamma \delta p(\mathbf{w}\mathbf{n}_\Gamma)\,d\Gamma - \int_\Omega \delta p\nabla^T k_f(\rho_f\mathbf{b})\,d\Omega \quad (18)$$

$$\int_\Omega \delta T(\rho c)_{avg}\dot{T}\,d\Omega + \int_\Omega \delta T(\rho_f c_f[k_f(-\nabla p + \rho\mathbf{b})])\nabla T\,d\Omega + \int_\Omega \nabla\delta T k\nabla T\,d\Omega = \int_\Gamma \delta T(q'')\,d\Gamma$$

where q'' and $\mathbf{n}_\Gamma$ are the thermal flux and the unit outward normal vector of external boundary, respectively, as shown in Fig. 2. Note that the total stress $\boldsymbol{\sigma}$ in the first integral equation (18) must be replaced by $\boldsymbol{\sigma} = \boldsymbol{\sigma}' - \alpha p\mathbf{I}$, in which the effective stress $\boldsymbol{\sigma}'$ can be related to the total strain $\boldsymbol{\varepsilon}$ and the thermal strain $\boldsymbol{\varepsilon}^t$ in the constitutive relation of $\boldsymbol{\sigma}' = \mathbf{D}(\boldsymbol{\varepsilon} - \boldsymbol{\varepsilon}^t)$, i.e.

$$\int_\Omega (\nabla\delta\mathbf{u})^T : \boldsymbol{\sigma}\,d\Omega = \int_\Omega (\nabla\delta\mathbf{u})^T : \mathbf{D}(\boldsymbol{\varepsilon} - \boldsymbol{\varepsilon}^t)\,d\Omega - \int_\Omega (\nabla\delta\mathbf{u})^T : (\alpha p\mathbf{I})\,d\Omega \quad (19)$$

where $\mathbf{D}$ is the material property of solid skeleton. In what follows, the spatial and time domain discretization of THM integral equations (18) are derived using the X-FEM and generalized Newmark approaches.

4.1. Spatial discretization

In order to solve the integral equations (18), the extended finite element method is employed for the spatial discretization. To achieve this aim, the displacement, pressure and temperature fields are enriched using the analytical solution to make the approximations capable of tracking the discontinuities. Various enrichment functions can be used to enhance the approximation fields. In the thermo-hydro-mechanical modeling of impermeable discontinuity proposed here, the displacement field is enriched by the Heaviside and crack tip asymptotic functions, and the pressure and temperature fields are enriched by the Heaviside and appropriate asymptotic functions. The enriched approximation of the extended finite element method for the field variable $\varphi(\mathbf{x})$ can be approximated using the enhanced trial function $\varphi^h(\mathbf{x})$ as

$$\varphi(\mathbf{x}) \approx \varphi^h(\mathbf{x}) = \sum_{i=1}^n N_i(\mathbf{x})\bar{\varphi}_i + \sum_{i=1}^n N_i(\mathbf{x})\psi(x)\bar{a}_i + \sum_{i=1}^n\sum_{j=1}^m N_i(\mathbf{x})\Phi^j(\mathbf{x})\bar{b}_i^j \quad (20)$$

where n is the number of nodal points in the FEM approach, $N_i(\mathbf{x})$ is the standard shape function, $\psi(\mathbf{x})$ denotes the Heaviside enrichment function used for strong discontinuities, $\Phi^j(\mathbf{x})$ indicates the additional asymptotic enrichment functions depending on the tip singularity of the displacement, pressure, or temperature field, and m is the required number of asymptotic solution used as the enrichment functions. In order to achieve the Kronecker property of standard FEM shape functions, i.e. $\varphi(x_i) = \bar{\varphi}_i$ at the nodal point i, Eq. (20) can be rewritten as

$$\varphi(\mathbf{x}) \approx \varphi^h(\mathbf{x} = \sum_{i=1}^n N_i(\mathbf{x})\bar{\varphi}_i + \sum_{i=1}^n N_i(\mathbf{x})(\psi(\mathbf{x}) - \bar{\psi}_i)\bar{a}_i + \sum_{i=1}^n\sum_{j=1}^m N_i(\mathbf{x})\left(\Phi^j(\mathbf{x}) - \bar{\Phi}_i^j\right)\bar{b}_i^j \quad (21)$$

in which for the strong discontinuity, $\psi(\boldsymbol{x})$ is defined by the Heaviside step function $H(\boldsymbol{x})$ as

$$\psi(\boldsymbol{x}) = H(\boldsymbol{x}) = \begin{cases} +1 & \text{if } (\boldsymbol{x} - \boldsymbol{x}^*) \cdot \mathbf{n}_d \geqslant 0 \\ 0 & \text{otherwise} \end{cases} \tag{22}$$

where $\boldsymbol{x}^*$ is the point on the discontinuity which has the closest distance from the point $\boldsymbol{x}$, and $\mathbf{n}_d$ is the unit normal vector to the discontinuity at point $\boldsymbol{x}^*$, as shown in Fig. 2. In Eq. (21), $\Phi^j(\boldsymbol{x})$ is the tip asymptotic functions, which is defined based on the analytical solutions of displacement, pressure and temperature fields at the vicinity of singularity as

$$\Phi^u = \{\Phi^{u_1}, \Phi^{u_2}, \Phi^{u_3}, \Phi^{u_4}\} = \left\{ \sqrt{r}\sin\frac{\theta}{2}, \sqrt{r}\cos\frac{\theta}{2}, \sqrt{r}\sin\frac{\theta}{2}\sin\theta, \sqrt{r}\cos\frac{\theta}{2}\sin\theta \right\} \tag{23}$$

$$\Phi^p = \sqrt{r}\sin\frac{\theta}{2} \tag{24}$$

$$\Phi^t = \sqrt{r}\sin\frac{\theta}{2} \tag{25}$$

where θ is in the range of $[-\pi, \pi]$. It must be noted that the value of θ is computed by using the local tip coordinate and obtained by inserting $\theta = \alpha - \pi$. The discrete form of integral equations (18) can be obtained in the extended finite element model using the following test and trial functions for the displacement, pressure and temperature fields. Applying the enriched field (21), the trial functions $\mathbf{u}(\boldsymbol{x}, t)$, $p(\boldsymbol{x}, t)$ and $T(\boldsymbol{x}, t)$ can be defined as

$$\mathbf{u}(\boldsymbol{x}, t) \approx \mathbf{u}^h(\boldsymbol{x}, t) = \sum_{i=1}^{n} N_i^u \bar{u}_i + \sum_{i=1}^{n} N_i^u (H - \overline{H}_i)\bar{a}_i + \sum_{i=1}^{n}\sum_{j=1}^{4} N_i^u \left(\Phi^{u_j} - \overline{\Phi}_i^{u_j} \right)\bar{b}_i^j$$

$$p(\boldsymbol{x}, t) \approx p^h(\boldsymbol{x}, t) = \sum_{i=1}^{n} N_i^p \bar{p}_i + \sum_{i=1}^{n} N_i^p (H - \overline{H}_i)\bar{c}_i + \sum_{i=1}^{n} N_i^p (\Phi^p - \overline{\Phi}_i^p)\bar{d}_i \tag{26}$$

$$T(\boldsymbol{x}, t) \approx T^h(\boldsymbol{x}, t) = \sum_{i=1}^{n} N_i^t \overline{T}_i + \sum_{i=1}^{n} N_i^t (H - \overline{H}_i)\bar{e}_i + \sum_{i=1}^{n} N_i^t (\Phi^t - \overline{\Phi}_i^t)\bar{f}_i$$

The test functions $\delta\mathbf{u}(\boldsymbol{x}, t)$, $\delta p(\boldsymbol{x}, t)$ and $\delta T(\boldsymbol{x}, t)$ can be defined as

$$\delta\mathbf{u}(\boldsymbol{x}, t) \approx \delta\mathbf{u}^h(\boldsymbol{x}, t) = \sum_{i=1}^{n} N_i^u \delta\bar{u}_i + \sum_{i=1}^{n} N_i^u (H - \overline{H}_i)\delta\bar{a}_i + \sum_{i=1}^{n}\sum_{j=1}^{4} N_i^u \left(\Phi^{u_j} - \overline{\Phi}_i^{u_j} \right)\delta\bar{b}_i^j$$

$$\delta p(\boldsymbol{x}, t) \approx \delta p^h(\boldsymbol{x}, t) = \sum_{i=1}^{n} N_i^p \delta\bar{p}_i + \sum_{i=1}^{n} N_i^p (H - \overline{H}_i)\delta\bar{c}_i + \sum_{i=1}^{n} N_i^p (\Phi^p - \overline{\Phi}_i^p)\delta\bar{d}_i \tag{27}$$

$$\delta T(\boldsymbol{x}, t) \approx \delta T^h(\boldsymbol{x}, t) = \sum_{i=1}^{n} N_i^t \delta\overline{T}_i + \sum_{i=1}^{n} N_i^t (H - \overline{H}_i)\delta\bar{e}_i + \sum_{i=1}^{n} N_i^t (\Phi^t - \overline{\Phi}_i^t)\delta\bar{f}_i$$

In above relations, variables $\bar{a}_i$, $\bar{b}_i^j$, $\bar{c}_i$, $\bar{d}_i$, $\bar{e}_i$ and $\bar{f}_i$ are the additional degrees-of-freedom according to additional enrichment functions. N_i^u, N_i^p and N_i^t are the standard shape functions of displacement, pressure and temperature of node i. The matrix form of the enhanced element shape functions can be written as

$$\mathbf{N}_{\text{enh}}^u = \left[\mathbf{N}_{\text{std}}^u, \ \mathbf{N}_{\text{enr}}^a, \ \mathbf{N}_{\text{enr}}^b \right]$$

$$\mathbf{N}_{\text{enh}}^p = \left[\mathbf{N}_{\text{std}}^p, \ \mathbf{N}_{\text{enr}}^c, \ \mathbf{N}_{\text{enr}}^d \right] \tag{28}$$

$$\mathbf{N}_{\text{enh}}^t = \left[\mathbf{N}_{\text{std}}^t, \ \mathbf{N}_{\text{enr}}^e, \ \mathbf{N}_{\text{enr}}^f \right]$$

where $(N_{\text{enr}}^a)_i = (N_{\text{std}}^u)_i(H - \overline{H}_i)$, $\left(N_{\text{enr}}^b\right)_i^j = (N_{\text{std}}^u)_i\left(\Phi^{u_j} - \overline{\Phi}_i^{u_j}\right)$, $(N_{\text{enr}}^c)_i = (N_{\text{std}}^p)_i(H - \overline{H}_i)$, $\left(N_{\text{enr}}^d\right)_i = (N_{\text{std}}^p)_i(\Phi^p - \overline{\Phi}_i^p)$, $(N_{\text{enr}}^e)_i = (N_{\text{std}}^t)_i(H - \overline{H}_i)$, $\left(N_{\text{enr}}^f\right)_i = (N_{\text{std}}^t)_i(\Phi^t - \overline{\Phi}_i^t)$. Similarly, the derivatives of displacement shape functions can be defined by $\mathbf{B}_{\text{enh}}{}^u = [\mathbf{B}_{\text{std}}{}^u, \mathbf{B}_{\text{enr}}{}^a, \mathbf{B}_{\text{enr}}{}^b]$ with $(B_{\text{std}}^u)_{ji} = \partial(N_{\text{std}}^u)_i/\partial x_j$, $(B_{\text{enr}}^a)_{ji} = \partial(N_{\text{enr}}^a)_i/\partial x_j$ and $\left(B_{\text{enr}}^b\right)_{ji} = \partial\left(N_{\text{enr}}^b\right)_i/\partial x_j$.

Substituting the trial and test functions (26) and (27) into the weak form of governing equations (18) and considering the arbitrariness of displacement, pressure and temperature test functions, the following coupled set of equations can be obtained as

$$\begin{pmatrix} \mathbf{M}_{uu} & \mathbf{M}_{ua} & \mathbf{M}_{ub} \\ \mathbf{M}_{au} & \mathbf{M}_{aa} & \mathbf{M}_{ab} \\ \mathbf{M}_{bu} & \mathbf{M}_{ba} & \mathbf{M}_{bb} \end{pmatrix} \begin{Bmatrix} \ddot{\bar{\mathbf{u}}} \\ \ddot{\bar{\mathbf{a}}} \\ \ddot{\bar{\mathbf{b}}} \end{Bmatrix} + \begin{pmatrix} \mathbf{K}_{uu} & \mathbf{K}_{ua} & \mathbf{K}_{ub} \\ \mathbf{K}_{au} & \mathbf{K}_{aa} & \mathbf{K}_{ab} \\ \mathbf{K}_{bu} & \mathbf{K}_{ba} & \mathbf{K}_{bb} \end{pmatrix} \begin{Bmatrix} \bar{\mathbf{u}} \\ \bar{\mathbf{a}} \\ \bar{\mathbf{b}} \end{Bmatrix} - \begin{pmatrix} \mathbf{Q}_{up} & \mathbf{Q}_{uc} & \mathbf{Q}_{ud} \\ \mathbf{Q}_{ap} & \mathbf{Q}_{ac} & \mathbf{Q}_{ad} \\ \mathbf{Q}_{bp} & \mathbf{Q}_{bc} & \mathbf{Q}_{bd} \end{pmatrix} \begin{Bmatrix} \bar{\mathbf{p}} \\ \bar{\mathbf{c}} \\ \bar{\mathbf{d}} \end{Bmatrix} - \begin{pmatrix} \mathbf{W}_{ut} & \mathbf{W}_{ue} & \mathbf{W}_{uf} \\ \mathbf{W}_{at} & \mathbf{W}_{ae} & \mathbf{W}_{af} \\ \mathbf{W}_{bt} & \mathbf{W}_{be} & \mathbf{W}_{bf} \end{pmatrix} \begin{Bmatrix} \bar{\mathbf{T}} \\ \bar{\mathbf{e}} \\ \bar{\mathbf{f}} \end{Bmatrix} - \begin{Bmatrix} \mathbf{f}_u^{(1)} \\ \mathbf{f}_a^{(1)} \\ \mathbf{f}_b^{(1)} \end{Bmatrix} = \mathbf{0}$$

$$\begin{pmatrix} \widetilde{\mathbf{Q}}_{pu} & \widetilde{\mathbf{Q}}_{pa} & \widetilde{\mathbf{Q}}_{pb} \\ \widetilde{\mathbf{Q}}_{cu} & \widetilde{\mathbf{Q}}_{ca} & \widetilde{\mathbf{Q}}_{cb} \\ \widetilde{\mathbf{Q}}_{du} & \widetilde{\mathbf{Q}}_{da} & \widetilde{\mathbf{Q}}_{db} \end{pmatrix} \begin{Bmatrix} \dot{\bar{\mathbf{u}}} \\ \dot{\bar{\mathbf{a}}} \\ \dot{\bar{\mathbf{b}}} \end{Bmatrix} + \begin{pmatrix} \mathbf{H}_{pp} & \mathbf{H}_{pc} & \mathbf{H}_{pd} \\ \mathbf{H}_{cp} & \mathbf{H}_{cc} & \mathbf{H}_{cd} \\ \mathbf{H}_{dp} & \mathbf{H}_{dc} & \mathbf{H}_{dd} \end{pmatrix} \begin{Bmatrix} \bar{\mathbf{p}} \\ \bar{\mathbf{c}} \\ \bar{\mathbf{d}} \end{Bmatrix} + \begin{pmatrix} \widetilde{\mathbf{S}}_{pp} & \widetilde{\mathbf{S}}_{pc} & \widetilde{\mathbf{S}}_{pd} \\ \widetilde{\mathbf{S}}_{cp} & \widetilde{\mathbf{S}}_{cc} & \widetilde{\mathbf{S}}_{cd} \\ \widetilde{\mathbf{S}}_{dp} & \widetilde{\mathbf{S}}_{dc} & \widetilde{\mathbf{S}}_{dd} \end{pmatrix} \begin{Bmatrix} \dot{\bar{\mathbf{p}}} \\ \dot{\bar{\mathbf{c}}} \\ \dot{\bar{\mathbf{d}}} \end{Bmatrix} + \begin{pmatrix} \mathbf{R}_{pt} & \mathbf{R}_{pe} & \mathbf{R}_{pf} \\ \mathbf{R}_{ct} & \mathbf{R}_{ce} & \mathbf{R}_{cf} \\ \mathbf{R}_{dt} & \mathbf{R}_{de} & \mathbf{R}_{df} \end{pmatrix} \begin{Bmatrix} \dot{\bar{\mathbf{p}}} \\ \dot{\bar{\mathbf{e}}} \\ \dot{\bar{\mathbf{f}}} \end{Bmatrix} - \begin{Bmatrix} \mathbf{f}_p^{(2)} \\ \mathbf{f}_c^{(2)} \\ \mathbf{f}_d^{(2)} \end{Bmatrix} = \mathbf{0}$$

$$\begin{pmatrix} \mathbf{L}_{tt} & \mathbf{L}_{te} & \mathbf{L}_{tf} \\ \mathbf{L}_{et} & \mathbf{L}_{ee} & \mathbf{L}_{ef} \\ \mathbf{L}_{ft} & \mathbf{L}_{fe} & \mathbf{L}_{ff} \end{pmatrix} \begin{Bmatrix} \dot{\bar{\mathbf{T}}} \\ \dot{\bar{\mathbf{e}}} \\ \dot{\bar{\mathbf{f}}} \end{Bmatrix} + \begin{pmatrix} \mathbf{C}_{tt} & \mathbf{C}_{te} & \mathbf{C}_{tf} \\ \mathbf{C}_{et} & \mathbf{C}_{ee} & \mathbf{C}_{ef} \\ \mathbf{C}_{ft} & \mathbf{C}_{fe} & \mathbf{C}_{ff} \end{pmatrix} \begin{Bmatrix} \bar{\mathbf{T}} \\ \bar{\mathbf{e}} \\ \bar{\mathbf{f}} \end{Bmatrix} - \begin{Bmatrix} \mathbf{f}_t^{(3)} \\ \mathbf{f}_e^{(3)} \\ \mathbf{f}_f^{(3)} \end{Bmatrix} = \mathbf{0}$$

$$(29)$$

The X-FEM discretization equations (29) can be rewritten as

$$\mathbf{M}\ddot{\overline{\mathbb{U}}} + \mathbf{K}\overline{\mathbb{U}} - \mathbf{Q}\overline{\mathbb{P}} - \mathbf{W}\overline{\mathbb{T}} - \mathbf{F}^{(1)} = \mathbf{0}$$

$$\widetilde{\mathbf{Q}}\,\dot{\overline{\mathbb{U}}} + \mathbf{H}\overline{\mathbb{P}} + \widetilde{\mathbf{S}}\dot{\overline{\mathbb{P}}} + \mathbf{R}\dot{\overline{\mathbb{T}}} - \mathbf{F}^{(2)} = \mathbf{0} \qquad (30)$$

$$\mathbf{L}\dot{\overline{\mathbb{T}}} + \mathbf{C}\overline{\mathbb{T}} - \mathbf{F}^{(3)} = \mathbf{0}$$

where $\overline{\mathbb{U}} = \langle \bar{\mathbf{u}}, \bar{\mathbf{a}}, \bar{\mathbf{b}} \rangle$, $\overline{\mathbb{P}} = \langle \bar{\mathbf{p}}, \bar{c}, \bar{d} \rangle$ and $\overline{\mathbb{T}} = \langle \overline{\mathbf{T}}, \bar{\mathbf{e}}, \bar{\mathbf{f}} \rangle$ are the complete set of the standard and enriched degrees-of-freedom of displacement, pressure and temperature fields, respectively. In the X-FEM equations (29), the matrices and load vectors are defined as

$$\mathbf{M} = \int_{\Omega} (\mathbf{N}_{\text{enh}}^u)^T \rho \mathbf{N}_{\text{enh}}^u \, d\Omega$$

$$\mathbf{K} = \int_{\Omega} (\mathbf{B}_{\text{enh}}^u)^T \mathbf{D} \mathbf{B}_{\text{enh}}^u \, d\Omega$$

$$\mathbf{Q} = \int_{\Omega} (\mathbf{B}_{\text{enh}}^u)^T \alpha \mathbf{m} \mathbf{N}_{\text{enh}}^p \, d\Omega \qquad (31)$$

$$\mathbf{W} = \int_{\Omega} (\mathbf{B}_{\text{enh}}^u)^T \mathbf{D} \frac{1}{3} \beta \mathbf{m} \mathbf{N}_{\text{enh}}^t \, d\Omega$$

$$\mathbf{F}^{(1)} = \int_{\Omega} (\mathbf{N}_{\text{enh}}^u)^T \rho \mathbf{b} \, d\Omega + \int_{\Gamma} (\mathbf{N}_{\text{enh}}^u)^T \bar{\mathbf{t}} \, d\Gamma$$

and

$$\widetilde{\mathbf{Q}} = \int_{\Omega} (\mathbf{N}_{\text{enh}}^p)^T \alpha \mathbf{m}^T \mathbf{B}_{\text{enh}}^u \, d\Omega$$

$$\mathbf{H} = \int_{\Omega} (\nabla \mathbf{N}_{\text{enh}}^p)^T k_f (\nabla \mathbf{N}_{\text{enh}}^p) \, d\Omega$$

$$\widetilde{\mathbf{S}} = \int_{\Omega} (\mathbf{N}_{\text{enh}}^p)^T \frac{1}{Q^*} \mathbf{N}_{\text{enh}}^p \, d\Omega \qquad (32)$$

$$\mathbf{R} = \int_{\Omega} (\mathbf{N}_{\text{enh}}^p)^T \beta \mathbf{N}_{\text{enh}}^t \, d\Omega$$

$$\mathbf{F}^{(2)} = \int_{\Gamma} (\mathbf{N}_{\text{enh}}^p)^T \widetilde{q}_n \, d\Gamma - \int_{\Omega} \mathbf{N}_{\text{enh}}^p \nabla^T (k_f \rho_f \mathbf{b}) \, d\Omega$$

and

$$\mathbf{L} = \int_{\Omega} (\mathbf{N}_{\text{enh}}^t)^T (\rho c)_{avg} \mathbf{N}_{\text{enh}}^t \, d\Omega$$

$$\mathbf{C} = \int_{\Omega} (\nabla \mathbf{N}_{\text{enh}}^t)^T k \nabla \mathbf{N}_{\text{enh}}^t \, d\Omega + \int_{\Omega} \mathbf{N}_{\text{enh}}^t (\rho_f c_f [k_f(-\nabla p + \rho \mathbf{b})]) \nabla \mathbf{N}_{\text{enh}}^t \, d\Omega \qquad (33)$$

$$\mathbf{F}^{(3)} = \int_{\Gamma} (\mathbf{N}_{\text{enh}}^t)^T q_n'' \, d\Gamma$$

In above relations, q_n'' is the thermal flux on the boundaries, $\mathbf{m}$ is the vector of Dirac delta function defined as $\mathbf{m}^T = \langle 1\,1\,0\,1 \rangle$.

4.2. Time discretization

In order to complete the numerical solution of X-FEM equations, it is necessary to integrate the time differential equations (30) in time [60]. The generalized Newmark GN22 method is employed for the displacement field $\overline{\mathbb{U}}$ and GN11 method for the pressure field $\overline{\mathbb{P}}$ and temperature field $\overline{\mathbb{T}}$ as [61,62]

$$\ddot{\overline{\overline{\mathbb{U}}}}^{t+\Delta t} = \ddot{\overline{\overline{\mathbb{U}}}}^t + \Delta\ddot{\overline{\overline{\mathbb{U}}}}^t$$

$$\dot{\overline{\overline{\mathbb{U}}}}^{t+\Delta t} = \dot{\overline{\overline{\mathbb{U}}}}^t + \ddot{\overline{\overline{\mathbb{U}}}}^t\Delta t + \beta_1\Delta\ddot{\overline{\overline{\mathbb{U}}}}^t\Delta t \tag{34}$$

$$\overline{\overline{\mathbb{U}}}^{t+\Delta t} = \overline{\overline{\mathbb{U}}}^t + \dot{\overline{\overline{\mathbb{U}}}}^t\Delta t + \frac{1}{2}\ddot{\overline{\overline{\mathbb{U}}}}^t\Delta t^2 + \frac{1}{2}\beta_2\Delta\ddot{\overline{\overline{\mathbb{U}}}}^t\Delta t^2$$

and

$$\dot{\overline{\mathbb{P}}}^{t+\Delta t} = \dot{\overline{\mathbb{P}}}^t + \Delta\dot{\overline{\mathbb{P}}}^t$$

$$\overline{\mathbb{P}}^{t+\Delta t} = \overline{\mathbb{P}}^t + \dot{\overline{\mathbb{P}}}^t\Delta t + \bar{\beta}\Delta\dot{\overline{\mathbb{P}}}^t\Delta t \tag{35}$$

and

$$\dot{\overline{\mathbb{T}}}^{t+\Delta t} = \dot{\overline{\mathbb{T}}}^t + \Delta\dot{\overline{\mathbb{T}}}^t$$

$$\overline{\mathbb{T}}^{t+\Delta t} = \overline{\mathbb{T}}^t + \dot{\overline{\mathbb{T}}}^t\Delta t + \bar{\gamma}\Delta\dot{\overline{\mathbb{T}}}^t\Delta t \tag{36}$$

where β_1, β_2, $\bar{\beta}$ and $\bar{\gamma}$ are parameters, which are usually chosen in the range of 0 to 1. However, for unconditionally stability of the algorithm, it is required that $\beta_1 \geqslant \beta_2 \geqslant \frac{1}{2}$, $\bar{\beta} \geqslant \frac{1}{2}$, and $\bar{\gamma} \geqslant \frac{1}{2}$. In above relations, $\overline{\overline{\mathbb{U}}}^t$, $\dot{\overline{\overline{\mathbb{U}}}}^t$ and $\ddot{\overline{\overline{\mathbb{U}}}}^t$ denote the values of displacement, velocity and acceleration of the standard and enriched degrees of freedom at time t, $\overline{\mathbb{P}}^t$ and $\dot{\overline{\mathbb{P}}}^t$ are the values of pressure and gradient of pressure of the standard and enriched DOFs at time t, and $\overline{\mathbb{T}}^t$ and $\dot{\overline{\mathbb{T}}}^t$ are the values of temperature and gradient of temperature of the standard and enriched DOFs at time t. Substituting relations (34)–(36) into the space-discrete equations (30), the following nonlinear equation can be achieved as

$$\begin{pmatrix} \mathbf{M} + \frac{1}{2}\beta_2\Delta t^2\mathbf{K} & -\bar{\beta}\Delta t\mathbf{Q} & -\bar{\gamma}\Delta t\mathbf{W} \\ \beta_1\Delta t\widetilde{\mathbf{Q}} & \widetilde{\mathbf{S}} + \bar{\beta}\Delta t\mathbf{H} & \mathbf{R} \\ 0 & 0 & \mathbf{L} + \bar{\gamma}\Delta t\mathbf{C} \end{pmatrix} \begin{Bmatrix} \Delta\ddot{\overline{\overline{\mathbb{U}}}}^t \\ \Delta\dot{\overline{\mathbb{P}}}^t \\ \Delta\dot{\overline{\mathbb{T}}}^t \end{Bmatrix} = \begin{Bmatrix} \mathbb{G}^{(1)} \\ \mathbb{G}^{(2)} \\ \mathbb{G}^{(3)} \end{Bmatrix} \tag{37}$$

where the right-hand-side of above equation denotes the vector of known values at time t defined as

$$\mathbb{G}^{(1)} = {}^{t+\Delta t}\mathbf{F}^{(1)} - \mathbf{M}\ddot{\overline{\overline{\mathbb{U}}}}^t - \mathbf{K}(\overline{\overline{\mathbb{U}}}^t + \dot{\overline{\overline{\mathbb{U}}}}^t\Delta t + \frac{1}{2}\ddot{\overline{\overline{\mathbb{U}}}}^t\Delta t^2) + \mathbf{Q}(\overline{\mathbb{P}}^t + \dot{\overline{\mathbb{P}}}^t\Delta t) + \mathbf{W}(\overline{\mathbb{T}}^t + \dot{\overline{\mathbb{T}}}^t\Delta t)$$

$$\mathbb{G}^{(2)} = {}^{t+\Delta t}\mathbf{F}^{(2)} - \widetilde{\mathbf{Q}}(\dot{\overline{\overline{\mathbb{U}}}}^t + \ddot{\overline{\overline{\mathbb{U}}}}^t\Delta t) - \mathbf{H}(\overline{\mathbb{P}}^t + \dot{\overline{\mathbb{P}}}^t\Delta t) - \widetilde{\mathbf{S}}\dot{\overline{\mathbb{P}}}^t - \mathbf{R}\dot{\overline{\mathbb{T}}}^t \tag{38}$$

$$\mathbb{G}^{(3)} = {}^{t+\Delta t}\mathbf{F}^{(3)} - \mathbf{L}\dot{\overline{\mathbb{T}}}^t - \mathbf{C}(\overline{\mathbb{T}}^t + \dot{\overline{\mathbb{T}}}^t\Delta t)$$

The set of nonlinear equations (37) can be solved using an appropriate approach, such as the Newton–Raphson procedure.

5. Numerical simulation results

In order to illustrate the accuracy and versatility of the extended finite element method in thermo-hydro-mechanical modeling of deformable porous media, several numerical examples are presented. The first two examples are chosen to illustrate the robustness and accuracy of computational algorithm for two benchmark problems. The first example illustrates the accuracy of X-FEM model in the heat transfer analysis of a plate with an inclined crack. The second example deals with the thermo-mechanical analysis of a plate with an edge crack to verify the stress intensity factor obtained from the numerical analysis with that reported by the analytical solution. In the third example, the X-FEM technique is performed in the hydro-mechanical analysis of an impermeable discontinuity in the saturated porous media. Finally, the last two examples are chosen to demonstrate the performance of proposed computational algorithm for the thermo-hydro-mechanical modeling of deformable porous media in two challenging problems. The fourth example illustrates the performance of the XFEM–THM technique for an inclined fault in the porous media with various fault angles. In the last example, the capability of proposed technique is presented for the randomly generated faults in saturated porous media.

5.1. A plate with an inclined crack in thermal loading

The first example is of a plate with an inclined crack subjected to thermal loading, as shown in Fig. 3. This example was modeled by Duflot [57] and Zamani et al. [58] to present their X-FEM formulation in the thermo-elastic fracture analysis. A rectangular plate of 2 m × 1 m is modeled with the crack length of 0.6 m located with θ = 30° at the center of plate. The prescribed temperatures of +20 °C and −20 °C are implied on the upper and lower edges of the plate, respectively. It is assumed that the normal flux from the left and right edges of the plate is zero, and the heat conductivity is equal to 837 w/m °C. A structured uniform mesh of 61 × 31 is used for the X-FEM analysis. In Fig. 4a, the distribution of temperature contour is shown for the steady state condition. The temperature contour is in complete agreement with that reported by Duflot [57] and Zamani et al. [58]. Obviously, the Heaviside enrichment function causes the jump in the thermal field at the crack faces. In Fig. 4b, the heat flux distribution is shown in the normal direction to crack, i.e. $-\mathit{k}\nabla T\mathbf{n}$, where the singularity can be
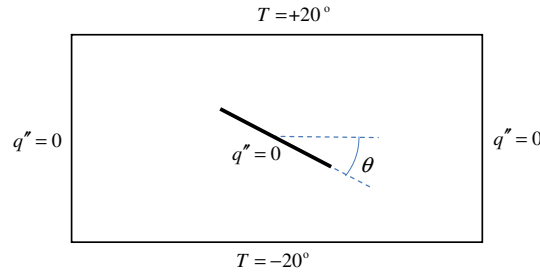
Fig. 3. Geometry and boundary condition of a plate with an inclined crack.
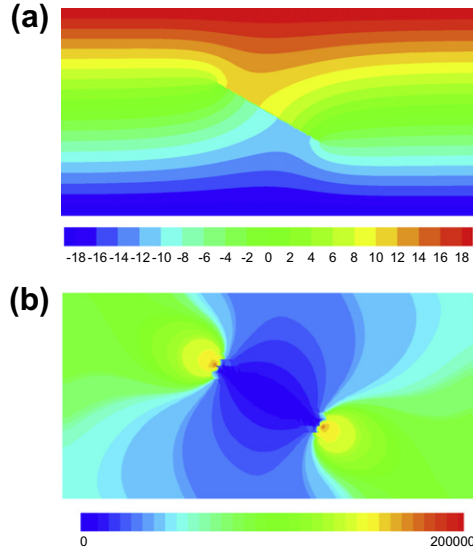

Fig. 4. A plate with an inclined crack: (a) the distribution of temperature; (b) the distribution of heat flux.

seen at both crack tips. Clearly, a good agreement can be seen between the proposed model and that reported by Zamani et al. [58].

5.2. A plate with an edge crack in thermal loading

The second example is a plate with an edge crack under thermal loading, as shown in Fig. 5a. This example is chosen to illustrate the accuracy of stress intensity factor obtained by the proposed X-FEM modeling of thermo-mechanical analysis. The derivation of stress intensity factor for the non-isothermal cracked domain is presented in Appendix A. A rectangular plate of 2.0 m × 0.5 m is assumed with an edge crack of 0.25 m at the mid-edge of plate. The prescribed temperatures of −50 °C and +50 °C are imposed at the left and right edges of the plate, respectively. A structured uniform X-FEM mesh of 20 × 80 is employed for the thermo-mechanical analysis in the plane strain condition. The material properties of the plate are given in Table 1. The coupled thermo-elasticity analysis is performed for 100 s. In order to illustrate the accuracy of proposed computational algorithm, the normalized stress intensity factor is compared with the analytical solution in Fig. 5b, in which the normalized SIF is obtained as

$$\mathscr{F} = \frac{3K_I}{\frac{E}{1-v}\beta\theta_0\sqrt{\pi a}} \tag{39}$$

in which, E is the elasticity module, a is the crack length, and θ_0 is the absolute value of the prescribed temperature applied at each edge of the plate. It can be seen from Fig. 5b that the steady state condition occurs after 20 s, where the normalized SIF value is equal to 0.492. Obviously, a good agreement can be seen between the computed value of normalized SIF (0.492) and the analytical value (0.495) reported by Duflot [57]. In Fig. 6, the distribution of temperature contour is shown at the end of simulation together with the displacement contours in x- and y-directions. According to the thermal boundary conditions, a contraction can be observed on the lower and upper edges of the crack. In Fig. 7, a comparison is performed between the
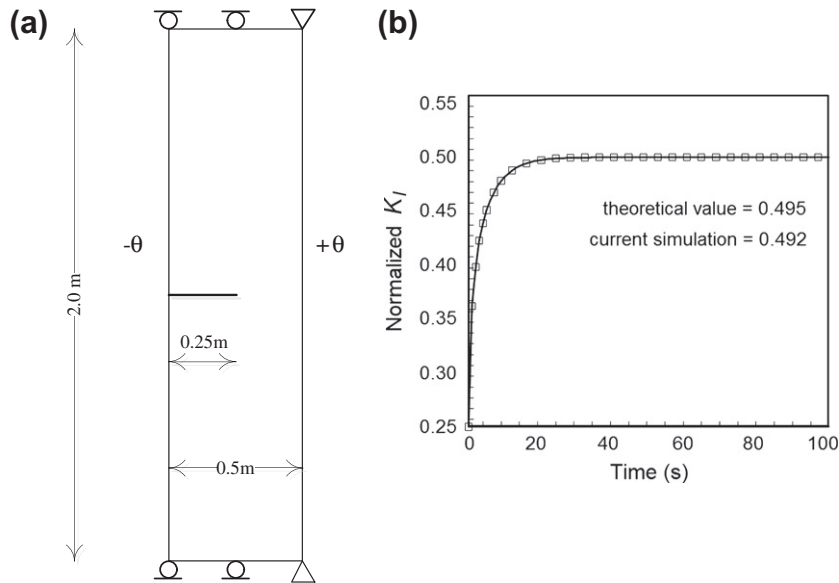
Fig. 5. A plate with an edge crack in thermal loading: (a) the geometry and boundary conditions; (b) the variation of normalized stress intensity factor with time.

Table 1
Material parameters for a plate with an edge crack in thermal loading.

Young module (kPa)	9×10^6
Poisson ratio	0.3
Solid density (kg/m³)	2×10^3
Thermal conductivity (W/m °C)	1×10^3
Volumetric thermal expansion coefficient (1/°C)	3×10^{-7}
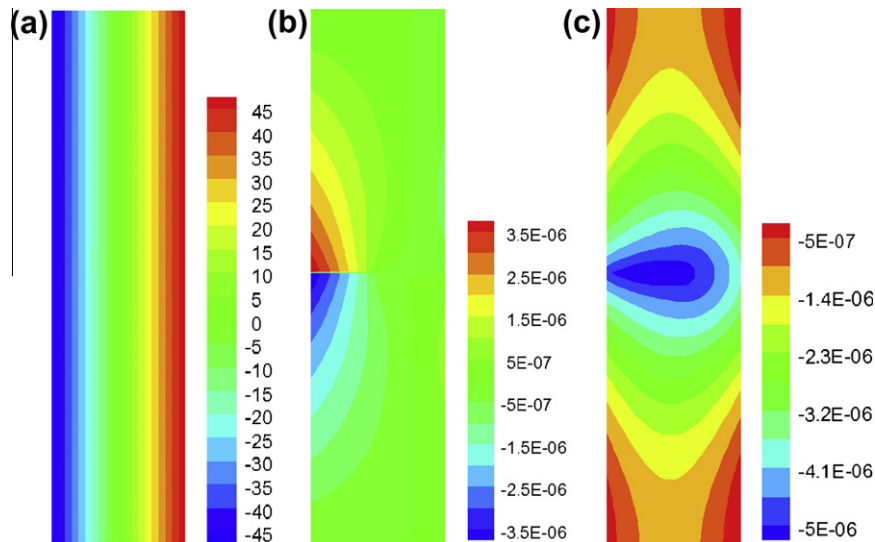
Fig. 6. A plate with an edge crack in thermal loading: (a) the distribution of temperature; (b) the displacement contour in y-direction; (c) the displacement contour in x-direction.

temperature obtained along the horizontal direction and that computed from the analytical solution [57] using $\theta(x) = (2x/w)\theta_0$, where $\theta(x)$ is the temperature distribution in the horizontal direction at the position of x from the crack-tip, and w is the width of the plate. A complete agreement can be seen between the numerical result and analytical solution.
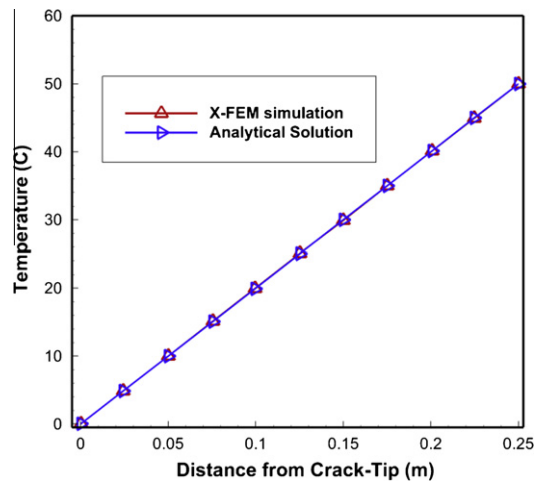
Fig. 7. The variation of temperature with the distance from crack-tip: a comparison between the numerical result and analytical solution.
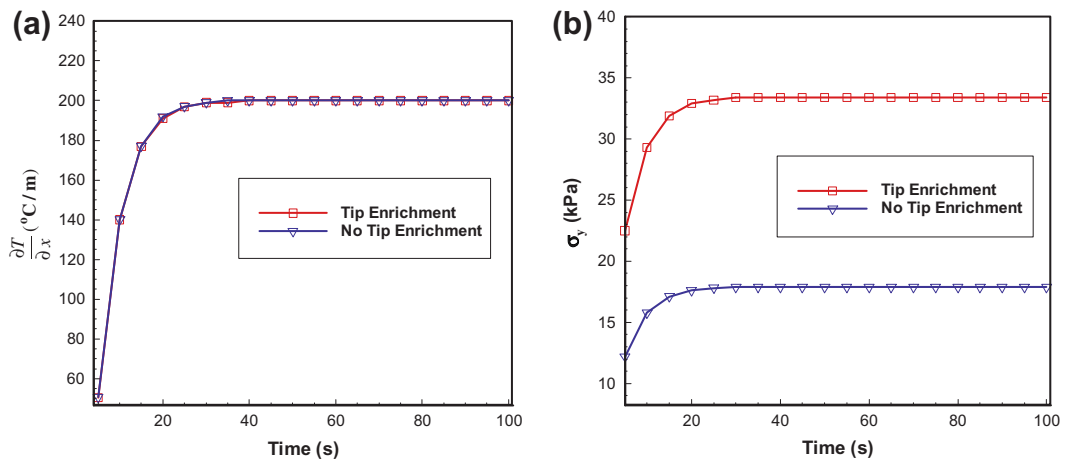
Fig. 8. The effect of crack-tip enrichment on: (a) the temperature gradient in x-direction; (b) the normal stress σ_y.
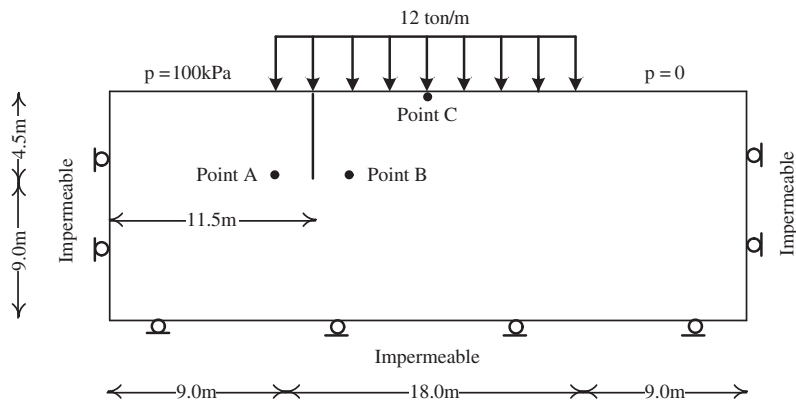
Fig. 9. An impermeable discontinuity in saturated porous media: the geometry and boundary conditions.

Table 2
Material parameters for an impermeable discontinuity in saturated porous media.

Young module (kPa)	9×10^6
Poisson ratio	0.4
Solid density (kg/m^3)	2×10^3
Fluid density (kg/m^3)	1×10^3
Porosity	0.3
Bulk module of fluid (MPa)	2×10^3
Bulk module of solid (MPa)	1×10^{14}
Permeability (m^2/Pa s)	1×10^{-9}
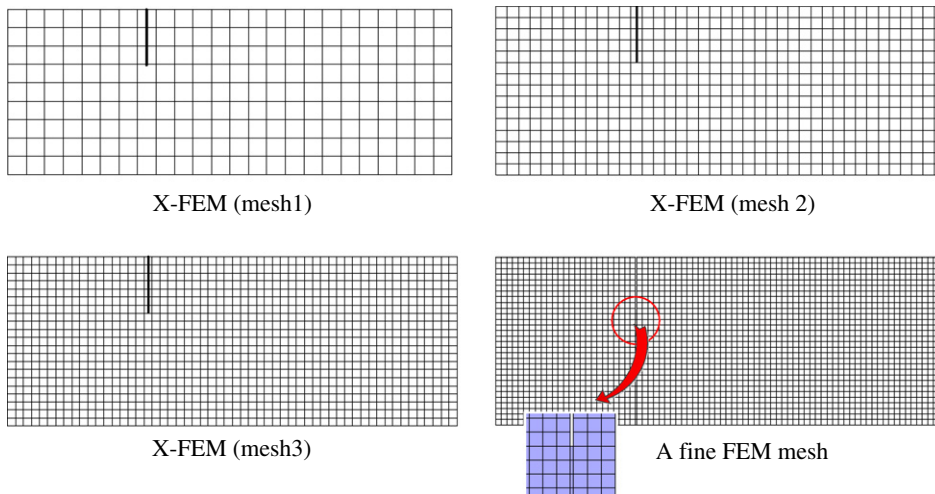
Fig. 10. Modeling of an impermeable discontinuity in saturated porous media using various X-FEM meshes.

In order to investigate the importance of crack-tip enrichment, the variations with time of the temperature gradient in x-direction and the normal stress σ_y are plotted in Fig. 8 at the crack-tip region with and without the tip enrichment function. Obviously, no difference can be observed in the heat flux curve between two different cases, as shown in Fig. 8a. The main reason is that the thermal streamlines are in the direction of crack edges, and the discontinuity cannot affect the heat flux paths. As a result, the enrichment degrees-of-freedom $\bar{f}_i$, defined in Eq. (26), have zero value and the results of temperature gradient between two different cases are identical. However, due to the increase of crack mouth opening, the tip enrichment function has significant affect in the normal stress σ_y, as shown in Fig. 8b.

5.3. An impermeable discontinuity in saturated porous media

In the next example, the performance of X-FEM model is presented in the hydro-mechanical analysis of an impermeable discontinuity in the fully saturated porous media, as shown in Fig. 9. In dam engineering problems, the sheet-pile is commonly used under the dam to decrease the pore pressure and hydraulic gradient at the downstream of the dam. In this example, the sheet-pile is considered as an impermeable discontinuity in the hydro-mechanical analysis of saturated porous media. The geometry and boundary conditions of the problem is shown in Fig. 9. A prescribed pressure of 100 kPa is assumed at the upstream, and zero pressure at the downstream. The soil is subjected to the distributed dam weight on the upper surface with the material properties given in Table 2. In order to investigate the effect of mesh size in X-FEM analysis, three X-FEM meshes are employed and the results are compared with a very fine FE mesh, as shown in Fig. 10. The analysis is performed for 110 s with the time increment of 0.1 s using the full Newton–Raphson method.

In Fig. 11, the distributions of pressure contour are shown in three time steps of $t = 5$, 10 and 110 s. In addition, the fluid flow streamlines are plotted in Fig. 11c at the end of simulation to illustrate the flow paths in the soil saturated medium. Clearly, the presence of impermeable discontinuity can be seen in the pressure contours around the sheet-pile. In Fig. 12a, the variations with time of the pressure are plotted for various X-FEM meshes at three points A, B and C, given in Table 3. In this figure, the pressure results are compared with the FEM technique that illustrates a remarkable agreement between the X-FEM and FEM approaches. In Fig. 12b, the variations with time of the vertical displacement are plotted for three X-FEM meshes at selected points. Obviously, the convergence can be seen among various X-FEM meshes when the size of elements is reduced. Also plotted in this figure are the variations with time of the vertical displacement for three points of
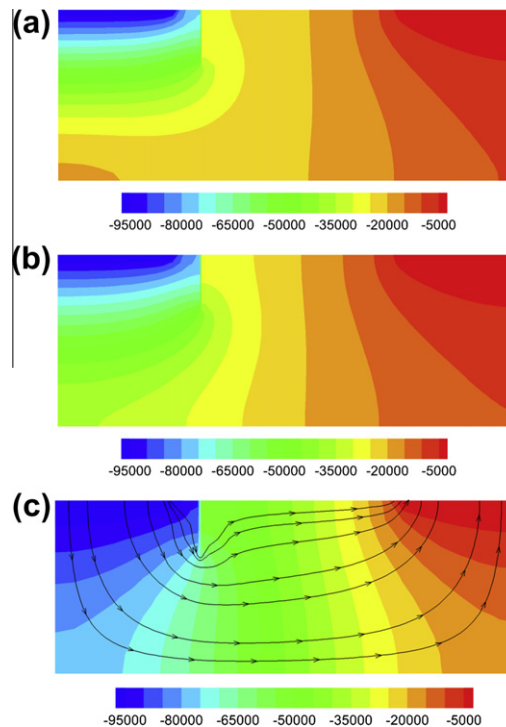
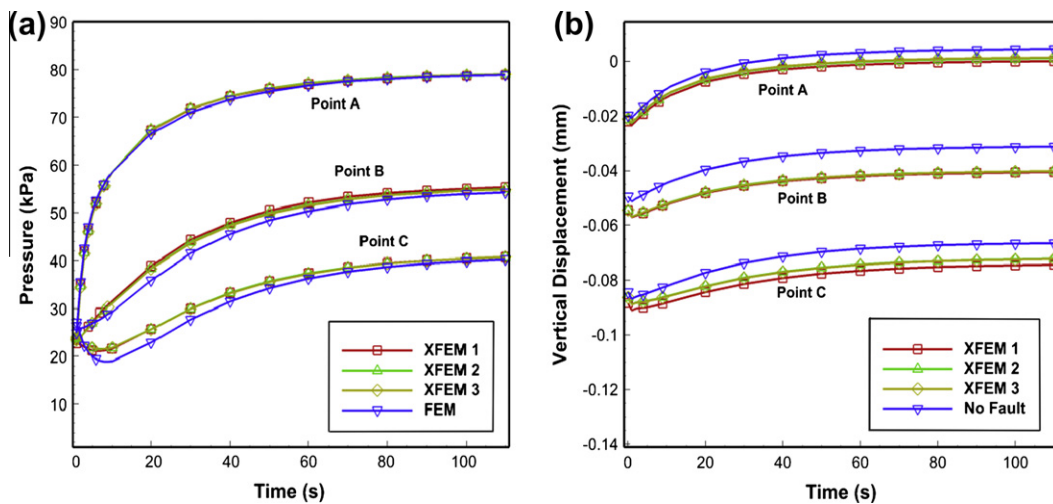Fig. 11. The distribution of pressure contours at time steps t = 5, 10 and 110 s.

Fig. 12. The variations with time of the pressure and vertical displacement at points A, B and C.

porous medium, where there is no fault in the domain. Clearly, the displacement curves display the influence of sheet-pile in reducing the uplift under the dam. In order to represent the importance of tip enrichment, the variations with time of the pressure and the gradient of pressure are plotted in Fig. 13 at the vicinity of singular point with and without the asymptotic enrichment function. Obviously, there is no difference in the curve of pressure between two different cases, as shown in Fig. 13a, however–the tip enrichment function has significant affect in the gradient of pressure, as shown in Fig. 13b.

5.4. An inclined fault in porous media

The next example refers to the X-FEM modeling of thermo-hydro-mechanical analysis of an inclined fault in the saturated porous media, as shown in Fig. 14. A square-shaped fractured domain of 10 m × 10 m is modeled in the plane strain

Table 3
Position of the points.

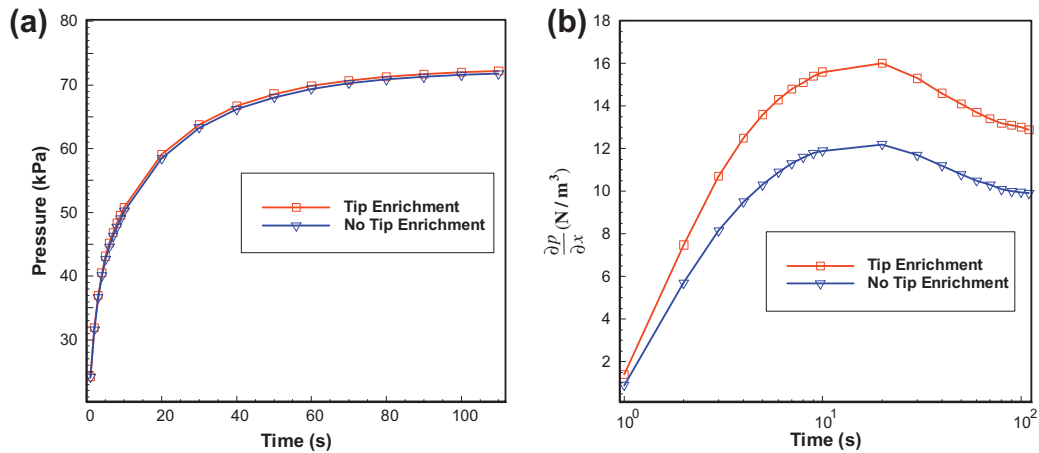|	x (m)	y (m)
Point A	9.0	9.0
Point B	13.5	9.0
Point C	18.0	13.5

Fig. 13. The effect of crack-tip enrichment on the pressure and the gradient of pressure at the normal direction to crack.
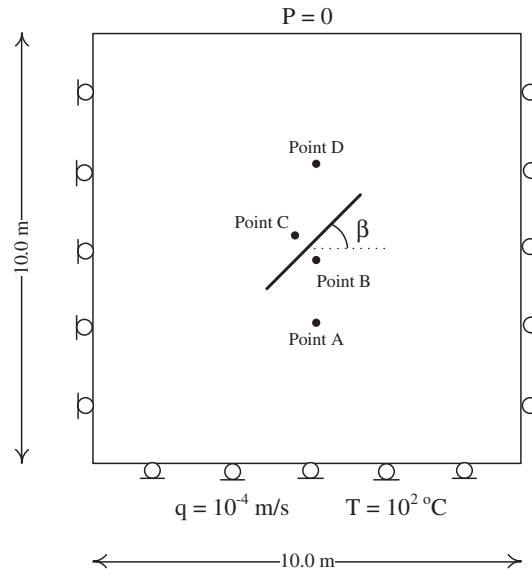

Fig. 14. An inclined fault in porous media: the geometry, boundary conditions and position of the fault.

condition, which is subjected to the prescribed temperature of 100 °C and a normal fluid flux of $q = 10^{-4}$ m/s at the bottom surface while the top surface is imposed as a drained condition with zero pressure and temperature. The geometry, boundary conditions and the position of the fault are shown in Fig. 11. The fault is assumed as an impermeable and adiabatic discontinuity with the length of 2 m located at the center of the domain. In Fig. 15, the uniform X-FEM mesh used in the thermo-hydro-mechanical analysis is shown. The material properties of the soil are given in Table 4. The problem is modeled for various fault angles $\beta = 0$, 30°, 45°, 60° and 90° to investigate the influence of pressure and temperature discontinuities over the domain. The simulation is performed for 10^5 s using the full Newton–Raphson method.
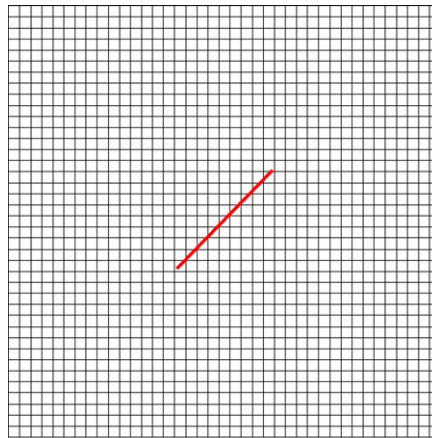
Fig. 15. The THM modeling of an inclined fault in porous media: the X-FEM mesh.

Table 4
Material parameters for an inclined fault in porous media.

Young module (kPa)	6×10^3
Poisson ratio	0.4
Solid density (kg/m^3)	2×10^3
Fluid density (kg/m^3)	1×10^3
Porosity	0.3
Bulk module of fluid (MPa)	2×10^3
Bulk module of solid (MPa)	1×10^{14}
Permeability (m^2/Pa s)	1.1×10^{-9}
Thermal conductivity of the bulk (W/m °C)	837
Solid specific heat (J/kg °C)	878
Fluid specific heat (J/kg °C)	4184
Volumetric thermal expansion coefficient (1/°C)	9.0×10^{-8}

In Fig. 16, the distributions of pressure and temperature contours are shown at the end of simulation for $\beta = 0°$ and 45°. Obviously, the pressure and temperature discontinuities can be seen along the fault, where the jump Heaviside enrichment function is applied in the thermal and pressure fields at the discontinuity faces. In Fig. 17, the variations with time of the pressure are plotted for different points given in Table 5, at various fault angles. It can be seen that the pressure increases in the domain due to the imposed fluid flux at the bottom surface, however, the fault causes the pressure discontinuity and prevents the fluid to flow directly through the domain. As a result, the variation of pressure decreases at points A and B (below the fault) when the fault angle increases, as shown in Fig. 17a and b. Conversely, the variation of pressure increases at points C and D (above the fault) when the fault angle increases, as shown in Fig. 17c and d. As it can be seen, the fluid can move freely toward the top surface in the case of vertical fault, because the fluid streamlines do not cross the discontinuity to affect their paths.

In Fig. 18, the variations with time of the temperature difference between points B and C (at both sides of the fault) are plotted for various fault angles. Obviously, at the initial time steps, i.e $t < 2 \times 10^4$ s, the temperature difference between points B and C increases to its maximum value, and then decreases because of the imposed temperature at the bottom surface. As can be expected, the variation of temperature difference (between points B and C) decreases when the fault angle increases. Obviously, in the case of vertical fault, the curve of $\beta = 90°$ is identical to that obtained from the domain with no fault. Finally, the effects of crack-tip enrichment are investigated in Fig. 19 for the pressure, temperature and their gradients at the crack-tip region in the case of $\beta = 45°$. In Fig. 19a and b, the variations with time of the pressure and pressure gradient are plotted at the crack-tip region with and without the pressure enrichment function. Also plotted in Fig. 19c and d are the variations with time of the temperature and temperature gradient at the crack-tip region with and without the temperature enrichment function. Obviously, the tip enrichment functions have significant affect in the gradient of pressure and temperature, as shown in Fig. 19b and d.

5.5. Randomly generated faults in saturated porous media

The last example is chosen to demonstrate the performance of proposed computational algorithm for the thermo-hydro-mechanical modeling of deformable porous media in a realistic problem, where a numbers of randomly generated faults are
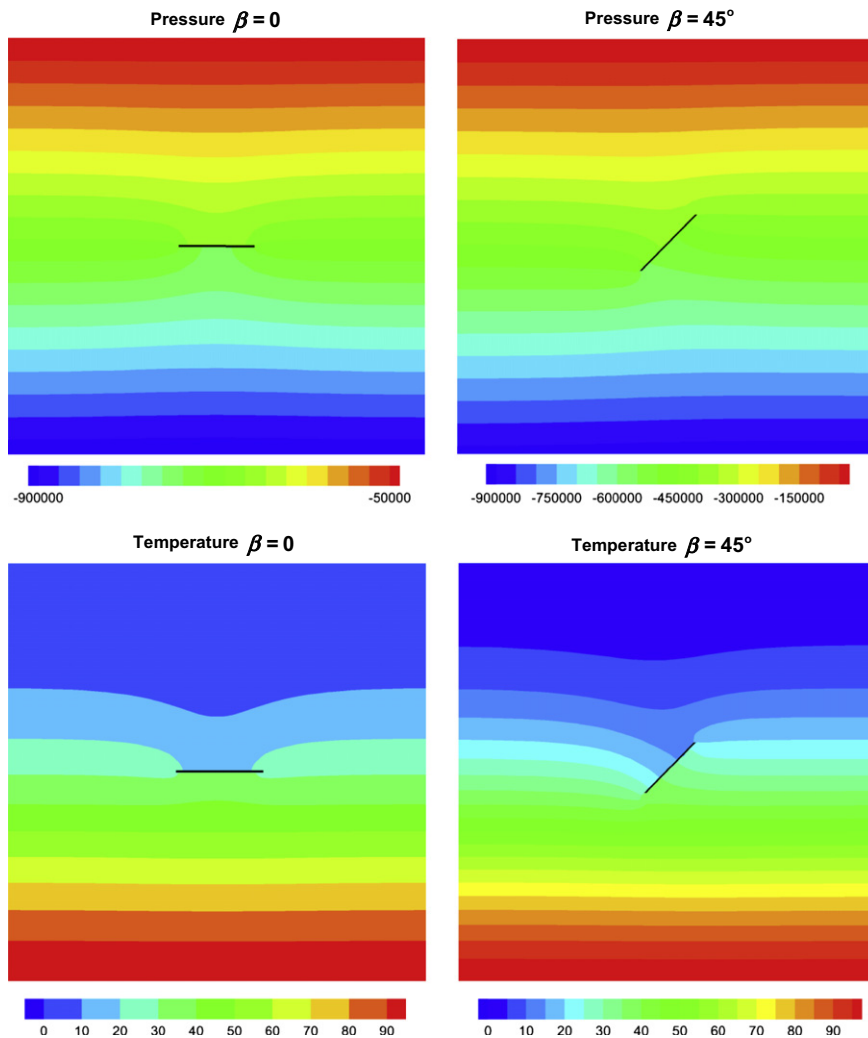
Fig. 16. The distributions of pressure and temperature contours at the end of simulation for $\beta = 0$ and $\beta = 45°$.

imposed in saturated porous media. Most of the in situ soils contain numerous impermeable materials, such as the hard stones distributed randomly in the media. In this example, the capability of proposed technique is presented for a set of six randomly generated faults in a saturated porous media, as shown in Fig. 20. The geometry, boundary conditions and the material parameters are considered similar to the previous example. The faults are assumed as impermeable and adiabatic discontinuities with different lengths and angles randomly distributed within the domain. The simulation is performed for 4×10^4 s, and the distribution of temperature and pressure contours are shown in Fig. 21 at the end of simulation. This figure clearly presents the influence of discontinuities on the distribution of temperature and pressure through the domain. Finally, the pressure streamlines for six randomly generated faults are plotted in Fig. 22. Obviously, the impermeable–adiabatic behavior of the faults prevents the fluid flow and the heat flux through the discontinuities in the domain. This example clearly presents the capability of X-FEM technique in the case of distinct enrichments in the thermo-hydro-mechanical media.

6. Conclusion

In the present paper, the extended finite element method was developed for numerical modeling of impermeable discontinuity in saturated porous media. In order to derive the thermo-hydro-mechanical governing equations, the momentum equilibrium equation, mass balance equation and the energy conservation relation were applied. The spatial discretization of governing equations of thermo-hydro-mechanical porous media was performed by the X-FEM technique, and followed by the generalized Newmark scheme for the time domain discretization. The displacement, pressure and temperature discon-
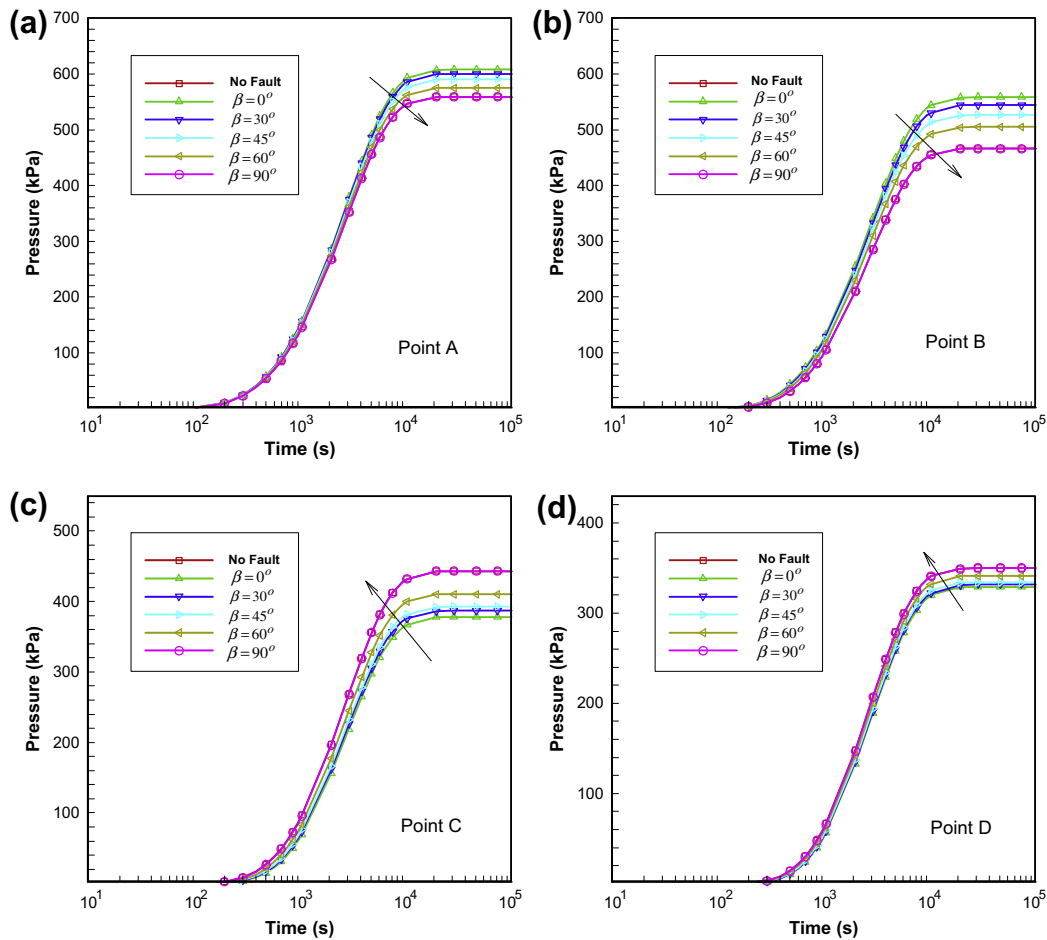
Fig. 17. The variations with time of the pressure for various fault angles at different points.

Table 5
Position of the points.

	x (m)	y (m)
Point A	5.13	3.85
Point B	5.13	4.87
Point C	4.87	5.13
Point D	5.13	6.15

tinuities were defined in porous media by enriching the displacement field using the Heaviside and crack tip asymptotic functions, and the pressure and temperature fields using the Heaviside and appropriate asymptotic functions.

Finally, numerical examples were analyzed to demonstrate the performance and capability of proposed computational algorithm in modeling of impermeable discontinuity in porous soils. The first example was chosen to illustrate the accuracy of X-FEM model in the heat transfer analysis of a plate with an inclined crack. The second example was selected to deal with the thermo-mechanical analysis of a plate with an edge crack to verify the stress intensity factor obtained from the numerical analysis with that reported by the analytical solution. The third example was chosen to perform the X-FEM hydro-mechanical analysis of an impermeable discontinuity in the saturated porous media. The last two examples were chosen to demonstrate the performance of proposed computational algorithm for the X-FEM thermo-hydro-mechanical modeling of deformable porous media in two challenging problems, including: an inclined fault in the porous media with various fault angles and the six randomly generated faults in saturated porous media. The distributions of pressure and temperature contours were shown at various time steps. In order to investigate the importance of tip enrichments, the variations with time of the pressure, temperature and their gradients were obtained at the vicinity of singular points with and without the asymp-
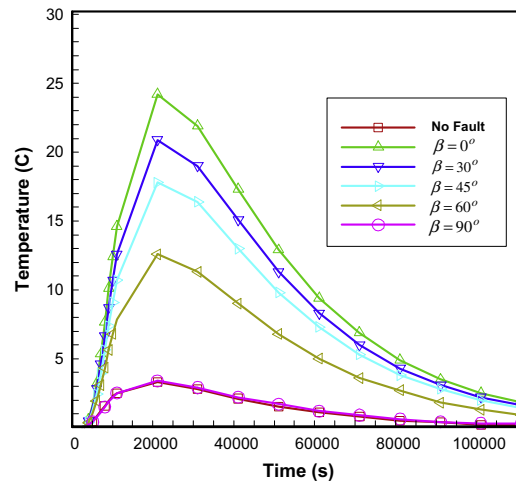
Fig. 18. The variations with time of the temperature difference between points B and C for various fault angles.
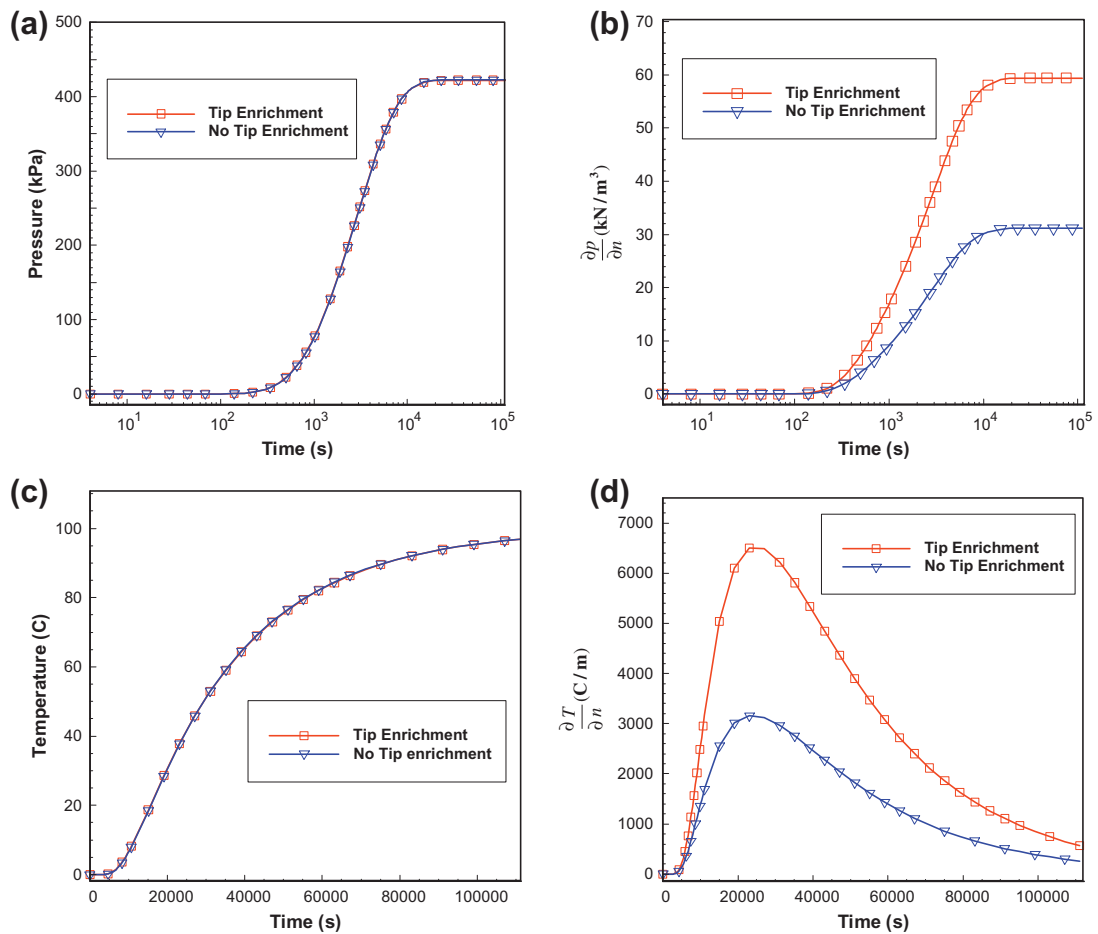

Fig. 19. The effect of crack-tip enrichment on the pressure and temperature and their gradients at the normal direction to the fault in the case of $\beta = 45°$.

totic enrichment functions. It was shown that the asymptotic enrichment functions have significant affects in the gradient of pressure and temperature, and as a result in the distribution of stress through the domain. It was shown how the XFEM–THM
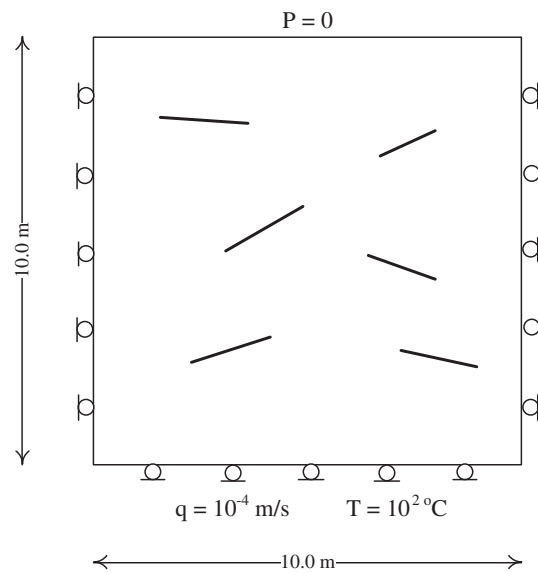
Fig. 20. Randomly generated faults in saturated porous media: the geometry, boundary conditions and position of faults.
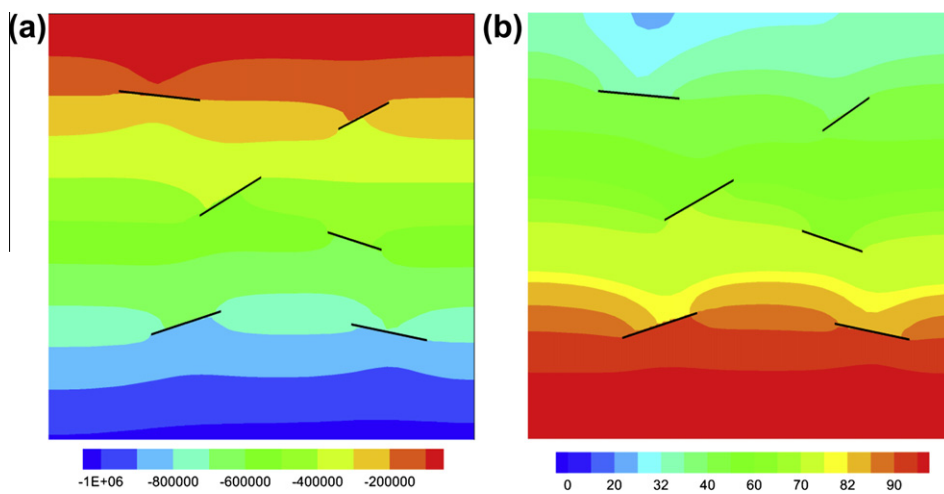

Fig. 21. Randomly generated faults in saturated porous media: (a) the distribution of pressure contour; (b) the distribution of temperature contour.
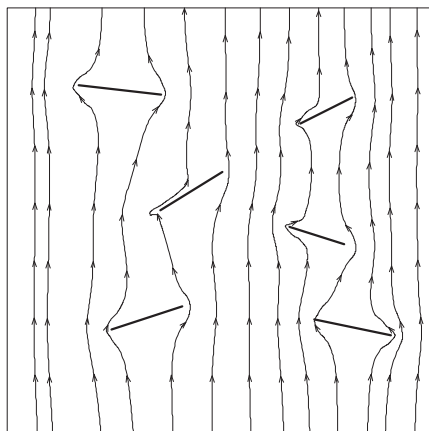

Fig. 22. The streamlines of the pressure for randomly generated faults in saturated porous media.

technique can be efficiently used to model the thermo-hydro-mechanical porous media with impermeable–adiabatic discontinuities.

Acknowledgment

Appendix A

A.1. Stress intensity factor in non-isothermal cracked domain

The stress intensity factor (SIF) in the non-isothermal cracked domain can be obtained using the interaction integral defined on the basis of J-integral as [57]

$$J = \int_{\Gamma_J} \mathbf{e}_1 \left[\frac{1}{2} \boldsymbol{\sigma} : (\boldsymbol{\varepsilon}^m)\mathbf{I} - (\nabla \mathbf{u})^T \boldsymbol{\sigma} \right] \mathbf{n}\, d\Gamma \tag{A.1}$$

where $\mathbf{e}_1$ is the normal unit vector in the local crack coordinate system, $\boldsymbol{\varepsilon}^m$ is the mechanical strain defined as $\boldsymbol{\varepsilon}^m = \boldsymbol{\varepsilon} - \boldsymbol{\varepsilon}^t$, with $\boldsymbol{\varepsilon}$ denoting the total strain, and $\mathbf{n}$ the outward normal to Γ_J (Fig. A.1). Considering two loading states (1) and (2) corresponding to the present state and auxiliary state, respectively, the interaction integral between these two states can be calculated by [58]

$$I^{(1,2)} = J^{(1+2)} - J^{(1)} - J^{(2)} \tag{A.2}$$

where $J^{(1)}$ and $J^{(2)}$ are the J-integrals corresponding to states (1) and (2), respectively, and $J^{(1+2)}$ is the J-integral in the combination of two states (1) and (2). Hence, relation (A.2) can be rewritten as

$$I^{(1,2)} = \int_{\Gamma_J} \mathbf{e}_1 [(\boldsymbol{\sigma}^{(1)} : \boldsymbol{\varepsilon}^{(2)})\mathbf{I} - ((\nabla \mathbf{u}^{(1)})^T \boldsymbol{\sigma}^{(2)} + (\nabla \mathbf{u}^{(2)})^T \boldsymbol{\sigma}^{(1)})]\mathbf{n}\, d\Gamma \tag{A.3}$$

In order to obtain the domain of above relation that is suitable for the numerical simulation, the region A is defined around the crack-tip with four boundaries Γ_J, Γ_{c+}, Γ_{c-} and Γ_e, as shown in Fig. A.1. Considering the virtual vector $\widehat{\mathbf{q}}$ defined as

$$\widehat{\mathbf{q}} = \begin{cases} \mathbf{e}_1 & \text{on } \Gamma_J \\ 0 & \text{on } \Gamma_e \\ \text{tangent} & \text{on } \Gamma_{c+} \text{ and } \Gamma_{c-} \\ \text{arbitrary} & \text{elsewhere} \end{cases} \tag{A.4}$$

and using the divergence theorem, relation (A.3) can be rewritten as

$$I^{(1,2)} = -\int_A \operatorname{div}\left\{ \widehat{\mathbf{q}} \left[(\boldsymbol{\sigma}^{(1)} : \boldsymbol{\varepsilon}^{(2)})\mathbf{I} - \left((\nabla \mathbf{u}^{(1)})^T \boldsymbol{\sigma}^{(2)} + (\nabla \mathbf{u}^{(2)})^T \boldsymbol{\sigma}^{(1)} \right) \right] \right\} dA \tag{A.5}$$
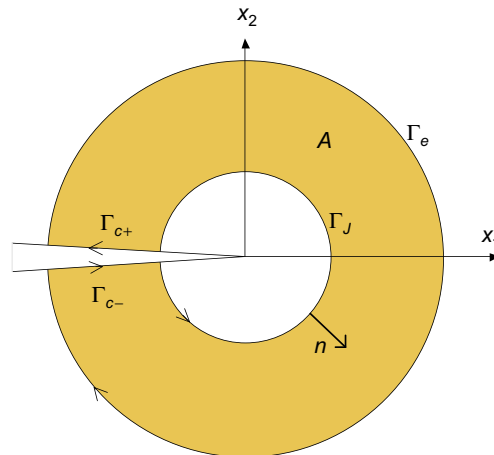

Fig. A.1. Notations for the crack tip integration.

By neglecting the body forces and considering the traction free crack faces, the interaction integral can be computed as

$$I^{(1,2)} = \int_A \nabla \widehat{\mathbf{q}} : \left[\left((\nabla \mathbf{u}^{(1)})^T \boldsymbol{\sigma}^{(2)} + (\nabla \mathbf{u}^{(2)})^T \boldsymbol{\sigma}^{(1)} \right) - (\boldsymbol{\sigma}^{(1)} : \boldsymbol{\varepsilon}^{(2)}) \mathbf{I} \right] dA + \int_A \widehat{\mathbf{q}} \left[\frac{\beta}{3} tr(\boldsymbol{\sigma}^{(1)}) \nabla T \right] dA \qquad (A.6)$$

In the mixed mode fracture mechanics, the J-integral is related to the stress intensity factors as

$$J = \frac{1}{E^*} \left(K_I^2 + K_{II}^2 \right) \qquad (A.7)$$

where $E^* = E$ for the plane stress and $E^* = E/(1 - v^2)$ for the plane strain problems. K_I and K_{II} are the modes I and II of the stress intensity factors, respectively. The interaction integral can be therefore obtained using the stress intensity factors in two states (1) and (2) as

$$I^{(1,2)} = \frac{2}{E^*} \left(K_I^{(1)} K_I^{(2)} + K_{II}^{(1)} K_{II}^{(2)} \right) \qquad (A.8)$$

In order to compute the SIF in mode I, the state field (2) is assumed as the pure mode I asymptotic solution, in which $K_I^{(2)} = 1$, $K_{II}^{(2)} = 0$ and $K_I^{(1)} = \frac{1}{2} E^* I^{(1,\text{mode I})}$. A similar process can be employed to compute the mode II stress intensity factor by considering the in-plane shear asymptotic solution for the auxiliary state.

References

[1] Gawin D, Klemm P. Coupled heat and moisture transfer with phase change in porous building materials. Arch Civil Engng 1994;40:89–104.
[2] Gawin D, Baggio P, Schrefler BA. Coupled heat, water and gas flow in deformable porous media. Int J Numer Meth Fluids 1995;20:969–87.
[3] Schrefler BA, Zhan XY, Simoni L. A coupled model for water flow, air flow and heat flow in deformable porous media. Int J Numer Meth Heat Fluid Flow 1995;5:531–47.
[4] Gawin D, Schrefler BA. Thermo-hydro-mechanical analysis of partially saturated porous materials. Engng Comput 1996;13:113–43.
[5] Vaziri HH. Theory and application of a fully coupled thermo-hydro-mechanical finite element model. Compos Struct 1996;61:131–46.
[6] Neaupane KM, Yamabe T. A fully coupled thermo-hydro-mechanical nonlinear model for a frozen medium. Comput Geotech 2001;28:613–37.
[7] Rutqvist J, Börgesson L, Chijimatsu M, Kobayashi A, Jing L, Nguyen TS, et al. Thermohydromechanics of partially saturated geological media: governing equations and formulation of four finite element models. Int J Rock Mech Min Sci 2001;38:105–27.
[8] Wang W, Kolditz O. Object-oriented finite element analysis of thermo-hydro-mechanical (THM) problems in porous media. Int J Numer Meth Engng 2007;69:162–201.
[9] Gatmiri B, Arson C. θ-STOCK, a powerful tool of thermohydromechanical behaviour and damage modeling of unsaturated porous media. Comput Geotech 2008;35:890–915.
[10] Chen Y, Zhou C, Jing L. Modeling coupled THM processes of geological porous media with multiphase flow: theory and validiation against laboratory and field scale experiments. Comput Geotech 2009;36:1308–29.
[11] Tong FG, Jing LR, Zimmerman RW. An effective thermal conductivity model of geological porous media for coupled thermo-hydro-mechanical systems with multiphase flow. Int J Rock Mech Min Sci 2009;46:1358–69.
[12] Tong FG, Jing LR, Zimmerman RW. A fully coupled thermo-hydro-mechanical model for simulating multiphase flow, deformation and heat transfer in buffer material and rock masses. Int J Rock Mech Min Sci 2010;47:205–17.
[13] Dumont M, Taibi S, Fleureau JM, AbouBekr N, Saouab A. Modelling the effect of temperature on unsaturated soil behaviour. Comp Rendus Geosci 2010;342:892–900.
[14] Noorishad J, Tsang CF, Witherspoon PA. Coupled thermal–hydraulic–mechanical phenomena in saturated fractured porous rock. J Geophys Res 1984;89:365–73.
[15] Boone TJ, Ingraffea AR. A numerical procedure for simulation of hydraulically-driven fracture propagation in poroelastic media. Int J Numer Anal Meth Geomech 1990;14:27–47.
[16] Remmers JJC, de Borst R, Needleman A. A cohesive segments method for the simulation of crack growth. Comput Mech 2003;31:69–77.
[17] Schrefler BA, Secchi S, Simoni L. On adaptive refinement techniques in multi-field problems including cohesive fracture. Comput Meth Appl Mech Engng 2006;195:444–61.
[18] Secchi S, Simoni L, Schrefler BA. Mesh adaptation and transfer schemes for discrete fracture propagation in porous materials. Int J Numer Anal Meth Geomech 2007;31:331–45.
[19] Radi E, Loret B. Mode II intersonic crack propagation in poroelastic media. Int J Fract 2007;147:235–67.
[20] Hoteit H, Firoozabadi A. An efficient numerical model for incompressible two-phase flow in fractured media. Adv Water Res 2008;31:891–905.
[21] Segura JM, Carol I. Coupled HM analysis using zero-thickness interface elements with double nodes. Part I: Theoretical model. Int J Numer Anal Meth Geomech 2008;32:2083–101.
[22] Remmers JJC, de Borst R, Needleman A. The simulation of dynamic crack propagation using the cohesive segment method. J Mech Phys Solids 2008;56:70–92.
[23] Khoei AR, Barani OR, Mofid M. Modeling of dynamic cohesive fracture propagation in porous saturated media. Int J Numer Anal Meth Geomech 2011;35:1160–84.
[24] Barani OR, Khoei AR, Mofid M. Modeling of cohesive crack growth in partially saturated porous media; a study on the permeability of cohesive fracture. Int J Fract 2011;167:15–31.
[25] Sarris E, Papanastasiou P. The influence of the cohesive process zone in hydraulic fracturing modeling. Int J Fract 2011;167:33–45.
[26] Carrier B, Granet S. Numerical modeling of hydraulic fracture problem in permeable medium using cohesive zone model. Engng Fract Mech 2012;79:312–28.
[27] Melenk JM, Babuska I. The partition of unity finite element method: basic theory and applications. Comput Meth Appl Mech Engng 1996;139:289–314.
[28] Belytschko T, Black T. Elastic crack growth in finite elements with minimal remeshing. Int J Numer Meth Engng 1999;45:601–20.
[29] Moës N, Dolbow J, Belytschko T. A finite element method for crack growth without remeshing. Int J Numer Meth Engng 1999;46:131–50.
[30] Daux C, Moës N, Dolbow J, Sukumar N, Belytschko T. Arbitrary branched and intersecting cracks with the extended finite element method. Int J Numer Meth Engng 2000;48:1741–60.
[31] Sukumar N, Chopp DL, Moës N, Belytschko T. Modeling holes and inclusions by level sets in the extended finite-element method. Comput Meth Appl Mech Engng 2001;190:6183–200.
[32] Belytschko T, Moës N, Usui S, Parimi C. Arbitrary discontinuities in finite elements. Int J Numer Meth Engng 2001;50:993–1013.
[33] Dolbow J, Moës N, Belytschko T. An extended finite element method for modeling crack growth with frictional contact. Comput Meth Appl Mech Engng 2001;190:6825–46.
[34] Wells GN, Sluys LJ. A new method for modeling cohesive cracks using finite elements. Int J Numer Meth Engng 2001;50:2667–82.

[35] Moës N, Belytschko T. Extended finite element method for cohesive crack growth. Engng Fract Mech 2002;69:813–33.
[36] Asferg JL, Poulsen PN, Nielson LO. A consistent partly cracked XFEM element for cohesive crack growth. Int J Numer Meth Engng 2007;72:464–85.
[37] Ventura G, Budyn E, Belytschko T. Vector level sets for description of propagating cracks in finite elements. Int J Numer Meth Engng 2003;58:1571–92.
[38] Areias PMA, Belytschko T. Analysis of three-dimensional crack initiation and propagation using the extended finite element method. Int J Numer Meth Engng 2005;63:760–88.
[39] Bordas S, Nguyen PV, Dunant C, Guidoum A, Nguyen-Dang H. An extended finite element library. Int J Numer Meth Engng 2007;71:703–32.
[40] Elguedj T, Gravouil A, Combescure A. Appropriate extended functions for X-FEM simulation of plastic fracture mechanics. Comput Meth Appl Mech Engng 2006;195:501–15.
[41] Khoei AR, Nikbakht M. An enriched finite element algorithm for numerical computation of contact friction problems. Int J Mech Sci 2007;49:183–99.
[42] Liu F, Borja R. A contact algorithm for frictional crack propagation with the extended finite element method. Int J Numer Meth Engng 2008;76:1489–512.
[43] Anahid M, Khoei AR. New development in extended finite element modeling of large elasto-plastic deformations. Int J Numer Meth Engng 2008;75:1133–71.
[44] Khoei AR, Biabanaki SOR, Anahid M. Extended finite element method for three-dimensional large plasticity deformations. Comput Meth Appl Mech Engng 2008;197:1100–14.
[45] Khoei AR, Anahid M, Shahim K. An extended arbitrary Lagrangian–Eulerian finite element method for large deformation of solid mechanics. Finite Elem Anal Des 2008;44:401–16.
[46] Khoei AR, Karimi K. An enriched-FEM model for simulation of localization phenomenon in Cosserat continuum theory. Comput Mater Sci 2008;44:733–49.
[47] de Borst R, Réthoré J, Abellan MA. A numerical approach for arbitrary cracks in a fluid-saturated medium. Arch Appl Mech 2006;75:595–606.
[48] Réthoré J, de Borst R, Abellan MA. A two-scale approach for fluid flow in fractured porous media. Int J Numer Meth Engng 2007;71:780–800.
[49] Khoei AR, Haghighat E. Extended finite element modeling of deformable porous media with arbitrary interfaces. Appl Math Model 2011;35:5426–41.
[50] Ren QW, Dong YW, Yu TT. Numerical modeling of concrete hydraulic fracturing with extended finite element method. Sci China Ser E-Tech Sci 2009;52:559–65.
[51] Lecampion B. An extended finite element method for hydraulic fracture problems. Commun Numer Meth Engng 2009;25:121–33.
[52] Mohamadnejad T, Khoei AR. An extended finite element method for fluid flow in partially saturated porous media with weak discontinuities; the convergence analysis of local enrichment strategies. Comput Mech, 2012. DOI 10.1007/s00466-012-0732-8.
[53] Mohamadnejad T, Khoei AR. Hydro-mechanical modeling of cohesive crack propagation in multi-phase porous media using the extended-FEM technique. Int J Numer Anal Meth Geomech 2012. http://dx.doi.org/10.1002/nag.2079.
[54] Fernandez RT. Natural convection from cylinders buried in porous media. PhD thesis, University of California; 1972.
[55] Lewis RW, Schrefler BA. The finite element method in the static and dynamic deformation and consolidation of porous media. Wiley; 1998.
[56] Yosibash Z. Numerical thermo-elastic analysis of singularities in two-dimensions. Int J Fract 1995;74:341–61.
[57] Duflot M. The extended finite element method in thermoelastic fracture mechanics. Int J Numer Meth Engng 2008;74:827–47.
[58] Zamani A, Gracie R, Eslami MR. Higher order tip enrichment of extended finite element method in thermoelasticity. Comput Mech 2010;46:851–66.
[59] Zamani A, Eslami MR. Implementation of the extended finite element method for dynamic thermoelastic fracture initiation. Int J Solids Struct 2010;47:1392–404.
[60] Khoei AR, Lewis RW, Zienkiewicz OC. Application of the finite element method for localized failure analysis in dynamic loading. Finite Elem Anal Des 1997;27:121–31.
[61] Khoei AR, Azami AR, Haeri SM. Implementation of plasticity based models in dynamic analysis of earth and rockfill dams: a comparison of Pastor-Zienkiewicz and cap models. Comput Geotech 2004;31:385–410.
[62] Khoei AR, Mohammadnejad T. Numerical modeling of multiphase fluid flow in deforming porous media: a comparison between two-and three-phase models for seismic analysis of earth and rockfill dams. Comput Geotech 2011;38:142–66.